Tectonophysics 717 (2017) 585–598

Contents lists available at ScienceDirect

Tectonophysics

journal homepage: www.elsevier.com/locate/tecto

Late Cenozoic cooling history of the central Menderes Massif: Timing of the Büyük Menderes detachment and the relative contribution of normal faulting and erosion to rock exhumation

Andreas Wölfler [a,*], Christoph Glotzbach [a,b], Caroline Heineke [c], Nils-Peter Nilius [a], Ralf Hetzel [c], Andrea Hampel [a], Cüneyt Akal [d], István Dunkl [e], Marcus Christl [f]

[a] Institute of Geology, Leibniz University of Hannover, Callinstraße 30, 30167 Hannover, Germany
[b] Department of Geoscience, University of Tübingen, Wilhelmstraße 56, 72074 Tübingen, Germany
[c] Institute of Geology and Palaeontology, University of Münster, Corrensstraße 24, 48149 Münster, Germany
[d] Dokuz Eylül University, Engineering Faculty, Department of Geological Engineering, Tınaztepe Campus, Buca, 35160, Izmir, Turkey
[e] University of Göttingen, Geoscience Center, Sedimentology and Environment Geology, Goldschmidstraße 3, 37077 Göttingen, Germany
[f] Laboratory of Ion Beam Physics, ETH Zurich, Otto-Stern-Weg 5, HPK G23, 8093 Zurich, Switzerland

ARTICLE INFO

Article history:
Received 14 July 2016
Received in revised form 27 June 2017
Accepted 9 July 2017
Available online 11 July 2017

Keywords:
Continental extension
Detachment faulting
Erosion
Low-temperature thermochronology
Cosmogenic nuclides

ABSTRACT

Based on new thermochronological data and ^{10}Be-derived erosion rates from the southern part of the central Menderes Massif (Aydın block) in western Turkey, we provide new insights into the tectonic evolution and landscape development of an area that undergoes active continental extension. Fission-track and (U-Th)/He data reveal that the footwall of the Büyük Menderes detachment experienced two episodes of enhanced cooling and exhumation. Assuming an elevated geothermal gradient of ~50 °C/km, the first phase occurred with an average rate of ~0.90 km/Myr in the middle Miocene and the second one in the latest Miocene and Pliocene with a rate of ~0.43 km/Myr. The exhumation rates between these two phases were lower and range from ~0.14 to ~0.24 km/Myr, depending on the distance to the detachment. Cosmogenic nuclide-based erosion rates for catchments in the Aydın block range from ~0.1 to ~0.4 km/Myr. The similarity of the erosion rates on both sides of the Aydın block (northern and southern flank) indicate that a rather symmetric erosion pattern has prevailed during the Holocene. If these millennial erosion rates are representative on a million-year timescale they indicate that, apart from normal faulting, erosion in the hanging wall of the Büyük Menderes detachment fault did also contribute to the exhumation of the metamorphic rocks.

1. Introduction

Low-angle normal faults play a crucial role for the exhumation of metamorphosed rocks from mid-crustal levels and usually form during late-orogenic extension (e.g. Dewey, 1988). Extensional settings have been intensively studied all over the world including the Basin-and-Range Province (e.g. Wernicke et al., 1988; Lister and Davis, 1989), the European Alps (e.g. Mancktelow, 1992; Selverstone, 1988; Campani et al., 2010; Scharf et al., 2013a) and the Aegean region (e.g. Lee and Lister, 1992; Gautier and Brun, 1994; Ring et al., 1999a; Brichau et al., 2006; Grasemann et al., 2012). The rapid cooling of metamorphic rocks exposed in these regions has commonly been interpreted to indicate that erosion has played a minor role to rock exhumation. However, the relative contribution of tectonic denudation and erosion to rock exhumation has rarely been quantified (e.g. Brichau et al., 2008; Buscher et al., 2013).

In the past decades, low-temperature thermochronology has proven to be a powerful tool to determine the cooling and exhumation history of rocks exhumed by detachment faulting (e.g. Dokka et al., 1986; Fitzgerald et al., 1991; Axen et al., 2000; Armstrong et al., 2003; Reiners and Ehlers, 2005). By using multiple thermochronometers with different closure temperatures, cooling paths can be constrained and converted into exhumation rates, provided the geo-thermal gradient can be satisfactorily approximated. To quantify rates of erosion, cosmogenic nuclides such as ^{10}Be can be used (Lal, 1991; Granger et al., 1996; von Blanckenburg, 2006). A combination of these methods allows resolving both the relative contribution of tectonic denudation and erosion to exhumation (e.g. Buscher et al., 2013). Since each method has a typical timescale over which it integrates, the multi-method approach is essential to gain quantitative insights into landscape evolution across different timescales.

* Corresponding author.
E-mail address: woelfler@geowi.uni-hannover.de (A. Wölfler).

http://dx.doi.org/10.1016/j.tecto.2017.07.004
0040-1951/

We conducted this study in the central Menderes Massif, an active extensional region in western Turkey (Fig. 1), which provides excellent exposures, including spectacular detachment faults, and quartz-bearing metamorphic rocks enabling the determination of ^{10}Be-based erosion rates. The metamorphic rocks of the central Menderes Massif are bound by two E-W-striking low-angle detachment faults: the Gediz detachment in the northern part of the Bozdağ block and the Büyük Menderes detachment in the southern part of the Aydın block (Fig. 1). Based on structural investigations and a limited set of apatite fission track ages it has been proposed that these two detachment faults were active during bivergent extension, which controlled the exhumation of the central Menderes Massif (Gessner et al., 2001a; Ring et al., 2003). A recent study by Buscher et al. (2013) combined several thermochronometers and cosmogenic nuclides to decipher the cooling and exhumation history of the metamorphic rocks in the Boz Dağ region in more detail (Fig. 1a). In contrast, the exhumation pattern of the Aydın block is only documented by a limited set of thermochronometers (Gessner et al., 2001a). Hence, to understand the history of faulting and bivergent extension in more detail, better temporal constraints on the exhumation of the Aydın block as well as on the timing of the Büyük Menderes detachment faulting are required. Here we present new apatite and zircon (U-Th)/He and fission-track ages as well as cosmogenic ^{10}Be data to place constraints on the cooling and erosion history of the Aydın block.

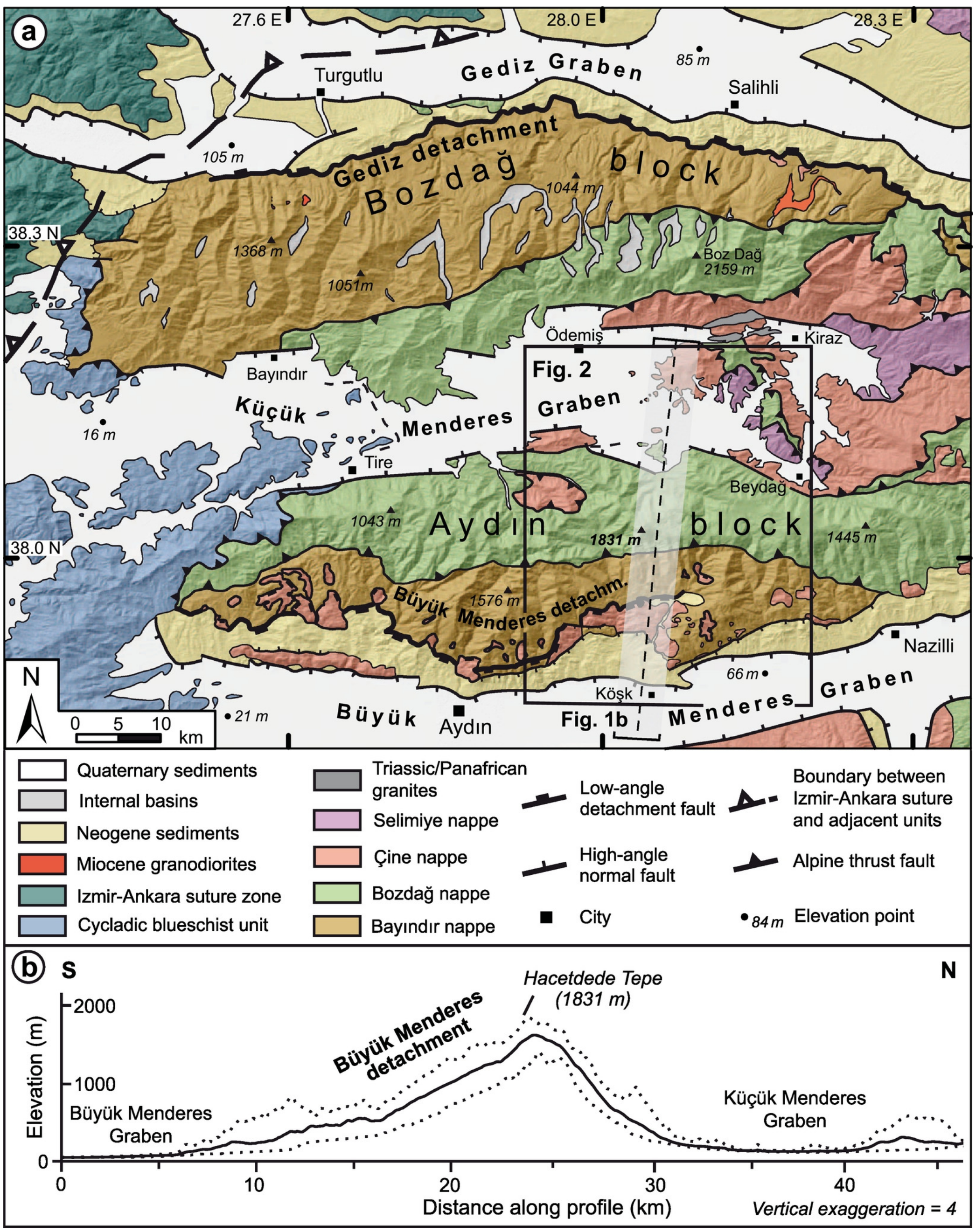

Fig. 1. (a) Geological map of the central Menderes Massif, western Turkey (compiled from Candan et al., 1992; Hetzel et al., 1995a; Hetzel et al., 1998; Gessner et al., 2001b; Özer and Sözbilir, 2003; Gürer et al., 2009; Candan et al., 2011; Koralay et al., 2011; Sözbilir et al., 2011; Gessner et al., 2013 and own field observations). (b) Swath profile across the Aydın block and the eastern Küçük Menderes Graben. Location is shown in (a). Note the topographic asymmetry of the Aydın block with the relative steep northern flank and the shallow-dipping Büyük Menderes detachment on its southern flank.

2. Geological setting of the central Menderes Massif

The Menderes Massif consists of a northern, central, and southern submassif, which are separated by tectonically active E-W trending graben systems (e.g. Seyitoğlu and Scott, 1991; Yılmaz et al., 2000; Bozkurt and Sözbilir, 2004). The central Menderes Massif can be divided into the northern Bozdağ and the southern Aydın block, which are separated by the Küçük Menderes Graben and bound by the Gediz and Büyük Menderes grabens in the north and south, respectively (Fig. 1). The main normal faults of the Gediz and Büyük Menderes grabens separate Neogene sediments in the footwalls from Quaternary sediments in the hanging walls (Çiftçi and Bozkurt, 2010; Gessner et al., 2013). Both graben-bounding faults are seismically active and have produced surface-rupturing earthquakes in 1899 and 1969 (Schaffer, 1900; Ambraseys, 1971; Eyidoğan and Jackson, 1985). The Küçük Menderes Graben is bound by steeply dipping normal faults, which were mainly active in the Pliocene and Quaternary (Rojay et al., 2005; Sümer, 2015). Although Miocene sediments are documented, the graben mainly developed in the Pliocene and Quaternary but has not experienced as much as extension as recorded in the Gediz and Büyük Menderes grabens (Gessner et al., 2001a; Gessner et al., 2013; Rojay et al., 2005).

The metamorphic rocks of the Menderes Massif consist of a nappe pile that formed by thrusting and crustal thickening during the Eocene (Şengör et al., 1984; Ring et al., 1999b; Ring et al., 2001; Regnier et al., 2003; Gessner et al., 2013). Available isotopic age data indicate that upper greenschist- to lower amphibolate-facies conditions occurred during Alpine metamorphism in late Eocene and Oligocene (Satir and Friedrichsen, 1986; Hetzel and Reischmann, 1996; Lips et al., 2001; Ring et al., 2003; Schmidt et al., 2015), although some rock units also experienced older, pre-Alpine phases of metamorphism (e.g. Bozkurt and Oberhänsli, 2001; Candan et al., 2001; Candan et al., 2011; Koralay, 2015). Here we use the tectonic subdivision of the Menderes Massif into four nappes, which was proposed by Gessner et al. (1998) and Ring et al. (1999b). According to these authors the nappe stack includes, from top to bottom, (1) the Selimiye nappe, (2) the Çine nappe, (3) the Bozdağ nappe, and (4) the Bayındır nappe (Figs. 1, 2). The Selimiye nappe mainly contains Paleozoic metapelites, metabasites, and marbles (e.g. Loos and Reischmann, 1999; Regnier et al., 2003; Gessner et al., 2004). The Çine nappe is made up of orthogneisses with intrusion ages of 560–530 Ma, metagranites, pelitic gneisses, and minor amphibolites and eclogites (e.g. Hetzel and Reischmann, 1996; Oberhänsli et al., 1997; Hetzel et al., 1998; Gessner et al., 2004; Zlatkin et al., 2012). The Bozdağ nappe mainly consists of mica schists and minor amounts of marbles and amphibolites (e.g. Koralay et al., 2001; Gessner et al., 2004; Candan et al., 2011). The metamorphic rocks of the Çine and Bozdağ nappes have Precambrian protolith ages (e.g. Candan et al., 2011; Gessner et al., 2001b; Gessner et al., 2004) and experienced high-grade metamorphism in Precambrian times (e.g. Bozkurt and Oberhänsli, 2001; Candan et al., 2001; Candan et al., 2011; Koralay, 2015). The Bayındır nappe contains mica schists, quarzites, phyllites, and marbles that were affected by greenschist-facies metamorphism in the Eocene (Lips et al., 2001; Özer and Sözbilir, 2003; Çemen et al., 2006). Fossils discovered in these marbles near the Büyük Menderes Graben document a Cretaceous depositional age and subsequent metamorphism during the Alpine orogenesis (Özer and Sözbilir, 2003).

Previous studies based on low-temperature thermochronology revealed a two-stage cooling history of the Menderes Massif (Gessner et al., 2001a; Ring et al., 2003; Işik et al., 2004; Thomson and Ring, 2006). The first stage occurred in the late Oligocene and early Miocene, when rocks of the northern and southern submassifs cooled to near-surface temperatures of ~110 °C (Ring et al., 2003; Thomson and Ring, 2006). The second stage is related to the late Miocene to Pliocene exhumation of the central Menderes Massif, which was driven by N-S to NNE-SSW directed extension along the Gediz and Büyük Menderes detachment faults (Fig. 1a) (e.g. Hetzel et al., 1995a, 1995b; Emre and Sözbilir, 1997; Gessner et al., 2001a; Bozkurt and Sözbilir, 2004).

The Gediz detachment dips about 15° to the NNE with a stretching lineation in the underlying mylonites plunging gently to the NNE (Hetzel et al., 1995a; Emre, 1996; Işik et al., 2003). The detachment was active from the middle Miocene until the Pliocene or possibly the early Quaternary (Buscher et al., 2013). The Büyük Menderes detachment is exposed along the southern flank of the central Menderes Massif (Figs. 1–3) as a mainly cataclastic shear zone with a dip of 0–15° and a top-to-the-S to SSW sense of movement (Gessner et al., 2001a) (Fig. 2c, d). So far, only a few apatite fission-track ages document early Miocene cooling of hanging wall units and late Miocene cooling of footwall units of the Büyük Menderes detachment, respectively (Gessner et al., 2001a; Ring et al., 2003).

The study area is located in the Aydın block, which exposes all four metamorphic nappes described above (Figs. 1, 2). The Aydın block is characterized by a pronounced topographic asymmetry, with a steep northern flank facing the Küçük Menderes Graben and a gently-dipping southern flank dominated by the Büyük Menderes detachment (Fig. 1b). The metamorphic rocks are overlain by faulted and northward tilted Neogene fluvio-lacustrine sediments (Figs. 1, 2) with northward dips of 15° to 30° (Fig. 2c). The oldest strata of the Neogene sediments are early to middle Miocene in age (Seyitoğlu and Scott, 1991; Sen and Seyitoğlu, 2009). The sediments are locally folded and overlain by undeformed Pliocene to Pleistocene sediments (Bozkurt, 2000, 2001). Historical earthquakes and geomorphological indicators such as well-preserved fault scarps document that the steep normal faults bounding the Büyük Menderes Graben to the north are still active (Fig. 2; Schaffer, 1900; Gürer et al., 2009). Active normal faulting on these steep faults is locally accompanied by hydrothermal activity and hot springs with temperatures of up to 100 °C (Karamanderesi and Helvacı, 2003).

3. Methods, sampling and sample preparation

3.1. Zircon and apatite fission-track analysis

We used the zircon and apatite fission-track (ZFT, AFT) methods, whose temperature sensitivity intervals are referred to as ZFT and AFT partial annealing zones, ranging from 380 to 190 °C and 120 to 60 °C, respectively (e.g. Wagner and van den Haute, 1992; Green et al., 1986; Rahn et al., 2004). Although closure temperatures can vary depending on factors such as cooling rate, chemistry, and accumulated radiation damage, typical closure temperatures for ZFT and AFT samples are ~240 °C and ~110 °C, respectively (Wagner and van den Haute, 1992; Gleadow and Duddy, 1981).

For fission-track analysis, we collected a total of 18 samples. Sample locations, lithologies, and structural positions are given in Fig. 2 and Table 1. Twelve samples are from the southern flank of the Aydın block (14M30–14M41). Eight of these samples are from the footwall of the Büyük Menderes detachment while the remaining four are from small augen gneiss klippen (i.e. remnants of the Çine nappe) in the hanging wall (Table 1). Five samples were taken from the northern flank of the Aydın block and one (14M23) from an augen gneiss unit exposed in the eastern Küçük Menderes Graben (Fig. 2a).

Zircon and apatite grains were separated using conventional magnetic and heavy liquid separation techniques and embedded in PDA Teflon™ and epoxy, respectively, grounded and polished. Zircon mounts were etched in a KOH-NaOH eutectic melt at 215 °C (Zaun and Wagner, 1985); the apatites were etched with 5 M HNO_3 for 20 s at 21 °C (Donelick et al., 1999). The samples were irradiated with thermal neutrons at the FRM-II reactor facility in Garching (Technical University Munich, Germany). Fission-track counting was carried out with an Olympus BX-51 microscope under 1000× magnification at the Institute of Geology in Hannover. We used the external detector method (Gleadow, 1981) with uranium-free muscovite sheets and the zeta calibration approach (e.g. Naeser, 1978; Hurford and Green, 1983) with dosimeter glass IRMM-540R and IRMM-541 and Durango apatite and Fish Canyon zircon age standards. For the assessment of annealing

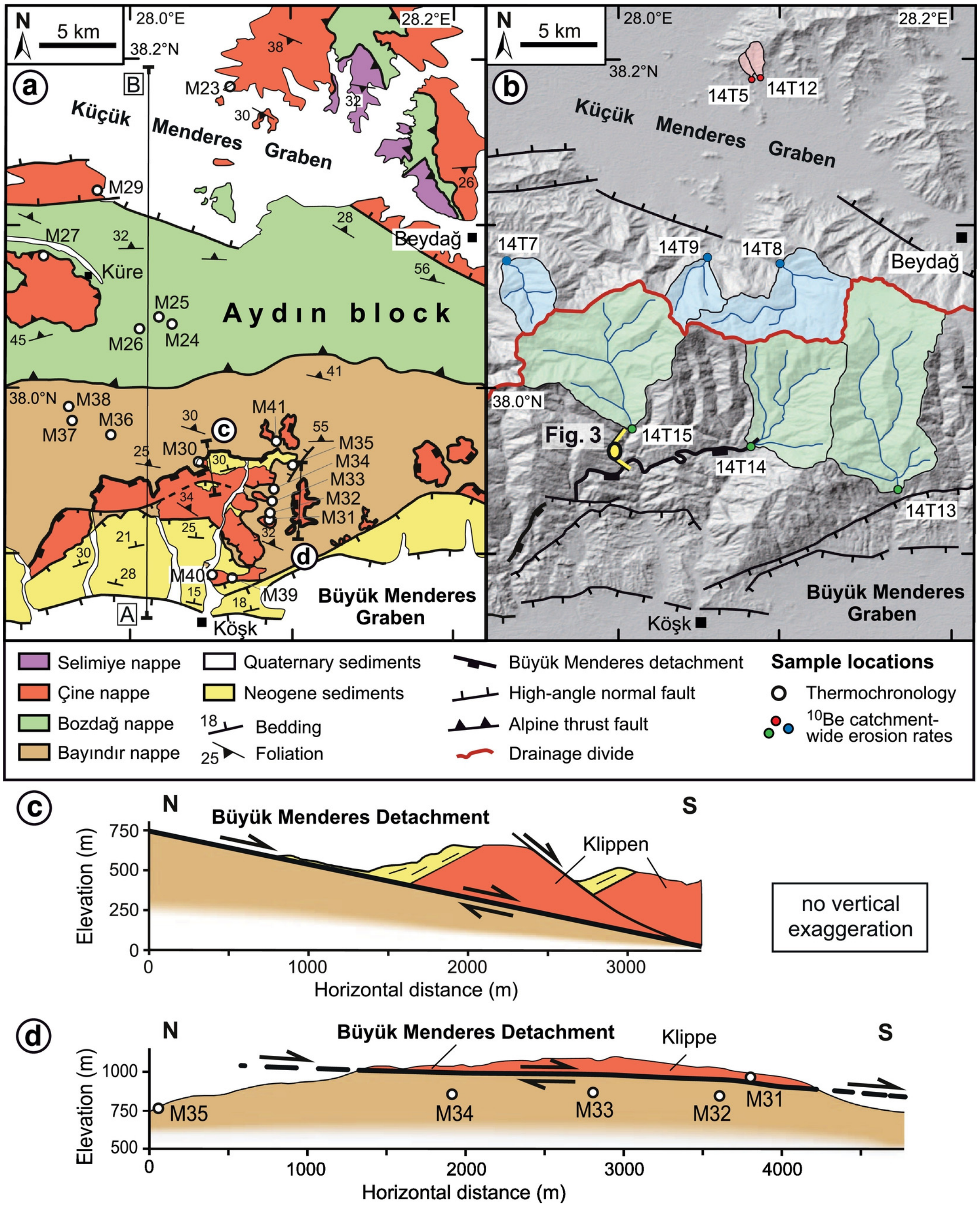

Fig. 2. (a, b) Geological map and shaded relief image of the study area north of Köşk. Note that both figures cover exactly the same region. The locations of the thermochronological samples are shown in the geological map (note that the first two numbers of the sample IDs (i.e. 14) are omitted for clarity). Rectangles with letters A and B denote the trace of the profile in Fig. 5. Bold letters in white circles (c and d) refer to the cross sections depicted below. The map is based on Candan et al., 1992; Emre and Sözbilir, 1997; Gürer et al., 2009; Hetzel et al., 1998; Özer and Sözbilir, 2003; Emre and Sözbilir, 2007; Candan et al., 2011; Koralay et al., 2011 and own field observations. The sampling sites for ^{10}Be-derived erosion rates and the respective catchments are indicated in the shaded-relief image. The yellow symbol near sample 14T15 indicates the view shown in the field photograph of Fig. 3. (c) N-S profile across the Büyük Menderes detachment. (d) Cross-section showing the flat-lying Büyük Menderes detachment. Sample 14M31 is from augen gneisses that occur in the hanging wall of the Büyük Menderes detachment.

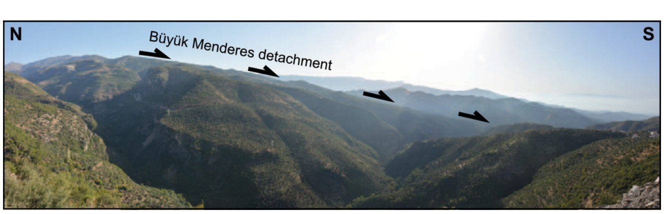

Fig. 3. Photograph of the Büyük Menderes detachment (for location see Fig. 2b). Black arrows delineate the detachment fault. Coordinates of viewpoint: 37.9584°N, 28.0000°E.

kinetics in apatites we used Dpar values (mean diameter of etch figures on prismatic surfaces of apatite parallel to the crystallographic c-axis) (Burtner et al., 1994). The mean track lengths from horizontal confined tracks were corrected for c-axis orientation (Donelick et al., 1999). Fission-track ages were calculated with the TRACKKEY software version 4.2 (Dunkl, 2002) and are reported in Tables 2 and 3 with 1σ errors.

3.2. Zircon and apatite (U-Th)/He analysis

Zircon and apatite (U-Th)/He thermochronology (ZHe, AHe) is based on the accumulation of radiogenic helium produced by the α-

Table 1
Location, lithology, and structural position of samples for low-temperature thermochronology.

Sample	Latitude (°N) (WGS 84)	Longitude (°E) (WGS 84)	Elevation (m)	Lithology	Structural position	Thermochronometers applied
14M23	38.1841	28.0610	135	Augen gneiss	Çine nappe	AHe, AFT, ZHe
14M24	38.0392	28.0265	1600	Paragneiss	Bozdağ nappe, footwall of Büyük Menderes detachment	AFT, ZHe
14M25	38.0438	28.0186	1187	Paragneiss	Bozdağ nappe, footwall of Büyük Menderes detachment	AFT, ZHe
14M26	38.0361	28.0066	887	Paragneiss	Bozdağ nappe, footwall of Büyük Menderes detachment	AFT, ZHe
14M27	38.0814	27.9482	556	Augen gneiss	Çine nappe	AFT, ZHe
14M29	38.1207	27.9806	177	Augen gneiss	Çine nappe	AHe, AFT, ZHe, ZFT
14M30	37.9553	28.0443	671	Augen gneiss	Çine nappe, hanging wall of Büyük Menderes detachment	AFT, ZHe
14M31	37.9227	28.0861	829	Augen gneiss	Çine nappe, hanging wall of Büyük Menderes detachment	AHe, AFT, ZHe, ZFT
14M32	37.9241	28.0864	830	Mica schist	Bayındır nappe, footwall of Büyük Menderes detachment	AFT, ZHe, ZFT
14M33	37.9310	28.0876	849	Mica schist	Bayındır nappe, footwall of Büyük Menderes detachment	AFT
14M34	37.9387	28.0884	831	Mica schist	Bayındır nappe, footwall of Büyük Menderes detachment	AHe, AFT, ZHe
14M35	37.9537	28.1034	766	Mica schist	Bayındır nappe, footwall of Büyük Menderes detachment	AHe, AFT, ZHe
14M36	37.9721	27.9892	846	Mica schist	Bayındır nappe, footwall of Büyük Menderes detachment	AFT, ZHe, ZFT
14M37	37.9803	27.9663	1087	Mica schist	Bayındır nappe, footwall of Büyük Menderes detachment	AHe, AFT, ZHe
14M38	37.9892	27.9641	1167	Mica schist	Bayındır nappe, footwall of Büyük Menderes detachment	AFT
14M39	37.8846	28.0630	287	Augen gneiss	Çine nappe, hanging wall of Büyük Menderes detachment	AFT, ZHe
14M40	37.8862	28.0476	181	Augen gneiss	Çine nappe, hanging wall of Büyük Menderes detachment	AHe, AFT
14M41	37.9682	28.0899	406	Mica schist	Bayındır nappe, footwall of Büyük Menderes detachment	AFT, ZHe

decay of ^{238}U, ^{235}U, ^{232}Th, and ^{147}Sm (e.g. Zeitler et al., 1987; Lippolt et al., 1994; Farley, 2002; Reiners et al., 2003). The temperature intervals at which helium diffusion approaches production (by alpha decay) is referred to as zircon and apatite helium partial retention zones with temperature ranges from 190 to 120 °C and 80 to 60 °C, respectively (Wolf et al., 1996, 1998; Farley, 2000; Reiners et al., 2003). The typical closure temperatures are 180 °C and 70 °C for the ZHe and AHe systems, respectively (Ehlers and Farley, 2003; Reiners et al., 2004; Reiners and Brandon, 2006; Flowers et al., 2007; Herman et al., 2007; Guenthner et al., 2013).

We employed (U-Th)/He dating on samples that yielded apatites and zircons of sufficient quality (Table 1). Apatite and zircon crystals were hand-picked using a stereo- and polarizing microscope and selected under 200× magnification following the selection criteria of Farley (2002) and Reiners (2005). The dimension of the selected crystals was measured to determine alpha-ejection correction factors (Farley et al., 1996). Single crystals were loaded into pre-cleaned Pt tubes for He analysis carried out at the GÖochron Laboratory at the University of Göttingen (Germany). Extraction of helium from crystals was performed by heating the encapsulated grains in vacuum using an IR laser. The extracted gas was purified by an SAES Ti-Zr getter and the He content was measured by a Hiden Hal-3F/PIC triple-filter quadrupole mass spectrometer. For measurements of the alpha-emitting elements U, Th, and Sm, the crystals were dissolved and spiked with calibrated ^{233}U, ^{230}Th, and ^{149}Sm solutions. Zircons were dissolved in Teflon bombs with 48% HF and 65% HNO_3 at 220 °C for five days. Apatites were dissolved in 2% ultrapure HNO_3 (+0.05% HF) in an ultrasonic bath. The actinide and Sm concentrations were measured by inductively coupled plasma mass spectrometry using the isotope dilution method with a Perkin Elmer Elan DRC II system equipped with an APEX microflow nebulizer. Errors for the single-grain ZHe and AHe analyses are attributed to uncertainties in the He, U, Th, and Sm measurements and the estimated uncertainty of the Ft correction factor. The zircon and apatite (U-Th)/He ages were calculated as unweighted mean ages from the single-grain ages of each sample and are reported in Tables 4 and 5 with an uncertainty of 2 standard errors.

3.3. Catchment-wide erosion rates from cosmogenic ^{10}Be

Spatially averaged erosion rates of river catchments can be determined from the ^{10}Be concentration in sand samples taken from active streams (e.g. Granger et al., 1996; von Blanckenburg, 2006). This approach assumes that the sediment in the stream channels is well mixed, that erosion is uniform through time, and that nuclide production in the catchment equals the outflux of nuclides via erosion and radioactive decay (e.g. Bierman and Steig, 1996).

To quantify spatially integrated erosion rates in the study area, we took stream sediment samples at the outlets of eight catchments that range in size between 1 and 102 km^2 (Fig. 2). Three samples were collected from streams draining the south-facing slope of the Aydın block, whereas three samples were taken from catchments that drain northwards into the Küçük Menderes graben (Fig. 2). The bedrock in these six catchments is dominated by greenschist- to amphibolite-facies mica schists, which constitute the main lithology in the Bozdağ and Bayındır nappes in this part of the Aydın block. We note that the three southern samples were taken relatively far upstream along the respective rivers to ensure that rocks of the Çine nappe are absent in these catchments. We also collected two samples from small ephemeral streams at the eastern end of the Küçük Menderes Graben (Fig. 2). These two catchments are entirely located in coarse-grained augen gneisses of the Çine nappe. In general, the position of all sampling

Table 2
Results of zircon fission track analyses.

Sample	Number of grains	ρs	Ns	ρi	Ni	ρd	Nd	P(χ^2) (%)	Dispersion	Central age ±1σ (Ma)	U (ppm)
14M29	20	75.474	717	92.737	881	6.815	2583	10	0.13	**30.3 ± 2.1**	607
14M31	20	75.225	835	96.757	1074	6.814	2583	8	0.13	**29.0 ± 1.9**	585
14M32	20	75.714	583	111.299	857	6.814	2583	61	0.04	**25.3 ± 1.7**	689
14M36	20	38.485	508	53.864	711	6.812	2583	0	0.32	**26.4 ± 2.6**	349

ρs (ρi) is the spontaneous (induced) track density (10^5 tracks/cm^2); Ns (Ni) is the number of counted spontaneous (induced) tracks; ρd is the dosimeter track density (10^5 tracks/cm^2); Nd is the number of tracks counted on the dosimeter; P(χ^2) is the probability of obtaining a Chi-square value (χ^2) for n degree of freedom (where n is the number of crystals minus 1); ages were calculated using the zeta calibration method (Hurford and Green, 1983), glass dosimeter IRMM541, and a zeta value of 109 ± 3 a/cm^2 calculated with Fish Canyon Tuff zircon standards.

Table 3
Results of apatite fission track analyses.

Sample	Number of grains	ρs	Ns	ρi	Ni	ρd	Nd	P(χ²) (%)	Dispersion	Central age ±1σ (Ma)	U (ppm)	Mean track length (μm)	SD (μm)	Number of track lengths measured	Dpar (μm)
14M23*	20	2.587	52	15.473	311	8.3118	3032	26	0	**17.7 ± 2.8**	26	13.78	1.20	34	1.56
14M24*	20	1.129	14	10.081	125	8.2999	3032	85	0	**11.8 ± 3.4**	18	12.98	0.88	50	1.57
14M25*	20	1.176	18	9.477	145	8.1326	3032	12	0.32	**13.1 ± 3.6**	15				1.79
14M26	20	2.665	105	20.787	819	8.276	3032	99	0	**12.4 ± 1.4**	37				1.68
14M27*	20	4.135	43	24.135	251	8.264	3032	90	0	**18.0 ± 3.1**	32	13.26	1.12	23	1.60
14M29*	20	3.254	82	17.143	432	8.2541	3032	0.11	0.56	**21.1 ± 3.8**	27	13.96	1.20	53	1.67
14M30*	20	2.586	30	13.621	158	8.2401	3032	85	0	**19.9 ± 4.0**	22	13.56	1.18	22	1.67
14M31*	15	2.887	41	17.042	242	8.2282	3032	50	0	**17.8 ± 3.1**	31	13.66	1.24	43	1.73
14M32*	15	0.655	11	16.190	272	8.2162	3032	77	0	**4.2 ± 1.3**	25				1.56
14M33	4	0.635	4	14.603	92	8.2034	3032	78	0	**4.2 ± 2.1**	28				1.57
14M34	17	0.512	19	11.402	423	8.1923	3032	2	0.67	**4.8 ± 1.4**	20				1.61
14M35*	11	0.788	7	15.444	139	8.1684	3032	50	0	**5.2 ± 2.0**	27				1.55
14M36	20	1.395	47	23.383	788	8.1565	3032	86	0	**5.7 ± 0.9**	41				1.53
14M37	20	1.762	77	12.586	550	8.145	3032	2	0.42	**14.7 ± 2.4**	21	13.09	1.11	16	1.64
14M38*	15	1.772	14	11.772	93	7.972	3032	99	0	**15.3 ± 4.4**	19	13.33	1.13	21	1.62
14M39	20	1.869	37	9.949	197	8.12	3032	9	0.54	**18.9 ± 4.2**	21	13.44	1.22	18	1.58
14M40*	20	0.649	32	2.677	132	8.1087	3032	12	0.61	**22.8 ± 5.8**	4	13.28	0.89	11	1.66
14M41	11	0.847	16	18.201	344	8.097	3032	29	0	**4.4 ± 1.1**	33				1.54

ρs (ρi) is the spontaneous (induced) track density (10^5 tracks/cm^2); Ns (Ni) is the number of counted spontaneous (induced) tracks; ρd is the dosimeter track density (10^5 tracks/cm^2); Nd is the number of tracks counted on the dosimeter; P(χ^2) is the probability of obtaining Chi-square value (χ^2) for n degree of freedom (where n is the number of crystals minus 1); ages were calculated using the zeta calibration method (Hurford and Green, 1983), glass dosimeter IRMM540, and zeta values of 235 ± 9 a/cm^2 (samples without asterisk) and 255 ± 9 a/cm^2 (samples with asterisk) calculated with Durango apatite standards.

sites, either at the boundary between the metamorphic rocks and the Neogene or Quaternary sediments or within the metamorphic rocks, ensures that the sediment source area of all samples encompasses only metamorphic rocks.

The 250–500 μm grain size fractions of the stream sediments obtained by sieving in the field were split into a magnetic and a non-magnetic fraction using a Frantz magnetic separator. The subsequent leaching procedure consisted of one etching step in 6 M HCl at 80 °C, four etching steps in dilute HF/HNO_3 in a heated ultrasonic bath (Kohl and Nishiizumi, 1992), and two alternating etching steps in aqua regia and 8 M HF to obtain pure quartz (Goethals et al., 2009). For beryllium extraction, ~0.3 mg of Be carrier was added to each sample. Following complete dissolution of quartz in HF (40%), samples were redissolved and converted into chloride form using 6 M HCl. Beryllium was separated by successive anion and cation exchange columns and precipitated as $Be(OH)_2$ at pH 8–9. Following the transformation to BeO at 1000 °C and target preparation for accelerator mass spectrometry (AMS), ^{10}Be was analyzed at the compact AMS facility "TANDY" of the ETH Zurich (Christl et al., 2013). The measured ^{10}Be/^{9}Be ratios are normalized to the secondary ETH standard S2007N with a nominal ^{10}Be/^{9}Be ratio of 28.1×10^{-12} (Kubik and Christl, 2010), considering the ^{10}Be half-life of 1.387 ± 0.012 Ma (Chmeleff et al., 2010; Korschinek et al., 2010). The secondary standard has been calibrated to the primary standard ICN 01-5-1 (Nishiizumi et al., 2007; Kubik and Christl, 2010).

Catchment-wide erosion rates were calculated from the blank-corrected ^{10}Be concentrations with the CRONUS-Earth online calculator (Balco et al., 2008; version 2.2; http://hess.ess.washington.edu) using the time-invariant production rate scaling model of Lal (1991) and Stone (2000) (Table 6). We note that the results of four samples (14T7, −8, −13 and −14) have been included in a manuscript that focusses on the lifetimes of water reservoirs in the Menderes Massif (Heineke et al., manuscript in revision). To account for the shielding of cosmic rays by the surrounding topography, a shielding factor was calculated for each catchment using the MATLAB script provided by Greg Balco (http://depts.washington.edu/cosmolab/shielding.m) and a digital elevation model with a horizontal resolution of 30 m (ASTER GDEM; http://www.gdem.aster.ersdac.or.jp). Erosion rates determined with cosmogenic nuclides approximately integrate over the time interval needed to remove a ~60 cm thick layer of bedrock from the surface: commonly a period of 10^3–10^5 years (e.g. Granger et al., 1996).

4. Results

4.1. Results from fission-track and (U-Th)/He analysis

The results from low-temperature thermochronology (Tables 2–5) reveal distinct ages for the rock samples from the footwall and hanging wall of the Büyük Menderes detachment fault, respectively (Fig. 4). The youngest ages are obtained from samples located below the Büyük Menderes detachment in the southern part of the study area (samples 14M32, −33, −34, −35, −36, −41). This group of samples yield AFT ages from 5.7 ± 0.9 to 4.2 ± 1.3 Ma and two AHe ages of 3.0 ± 0.3 Ma, respectively (Figs. 4, 5). The ZHe and ZFT ages of these samples are significantly older and range from 15.7 ± 3.6 to 12.2 ± 0.7 Ma and from 26.4 ± 2.6 to 25.3 ± 1.7 Ma, respectively (Figs. 4, 5). A second sample group is defined by footwall samples from the central and northern part of the Aydın block (14M24, −25, −26, −37, −38). AFT and ZHe ages of these samples range from 15.3 ± 4.4 to 11.8 ± 3.4 Ma and from 16.5 ± 0.8 to 13.0 ± 0.8 Ma, respectively. The third group of samples is defined by the oldest ages and comprises four augen gneiss samples from the hanging wall of the Büyük Menderes detachment (14M30, −31, −39, −40), one sample from the northern flank of the Aydın block (14M27), and two samples of augen gneisses in the Küçük Menderes Graben (14M23, −29). The two ZFT ages from this group are 30.3 ± 2.1 Ma and 29.0 ± 1.9 Ma, whereas the ZHe and AFT ages range from 25.7 ± 0.9 to 20.0 ± 1.6 Ma and from 22.8 ± 5.8 to 17.7 ± 2.8 Ma, respectively (black symbols in Fig. 5). The augen gneisses from the Küçük Menderes Graben yield AHe ages of 21.9 ± 1.2 Ma and 17.5 ± 1.7 Ma. In contrast, two samples from the hanging wall of the Büyük Menderes detachment (14M31, −40) yield AHe ages of 1.6 ± 0.2 and 0.5 ± 0.1 Ma (Fig. 5).

The apatite samples from all three age groups are characterized by unimodal track length distributions and relatively long mean track lengths (13.0 to 13.8 μm, with standard deviations of 0.9 to 1.2 μm) (Table 3). The track length data suggest a moderately fast cooling through the apatite partial annealing zone in the Miocene to Pliocene. Mean Dpar values of the samples range from 1.53 to 1.79 μm (Table 3), pointing to a homogeneous chemical composition of the samples, typical for fluorine-apatite.

By using the closure temperatures mentioned in Section 3 (i.e. ZFT: 240 °C, ZHe: 180 °C, AFT: 110 °C, AHe: 70 °C) and a mean annual surface

Table 4
Results of zircon (U-Th)/He geochronology.

Sample	Aliq.	He Vol.	1σ	^{238}U Mass	1σ	Conc.	^{232}Th Mass	1σ	Conc.	Th/U ratio	Sm Mass	1σ	Conc.	Ejection correction	Uncorr. age	FT-corr. age	2σ	Sample age	2se
		(10^{-9} cm^3)	(%)	(ng)	(%)	(ppm)	(ng)	(%)	(ppm)		(ng)	(%)	(ppm)		(Ma)	(Ma)	(Ma)	(Ma)	(Ma)
14M23	#1	2.105	1.2	1.132	1.8	499	0.134	2.4	59	0.12	0.031	7.6	14	0.68	15.0	**22.02**	2.30	**21.8**	0.3
	#2	4.243	1.1	2.340	1.8	829	0.103	2.4	37	0.04	0.005	18.5	2	0.69	14.9	**21.53**	2.19		
14M24	#1	1.551	1.2	1.128	1.8	268	0.410	2.4	98	0.36	0.010	12.7	2	0.80	10.5	**13.10**	0.95	**13.9**	1.3
	#2	1.081	1.2	0.850	1.8	276	0.345	2.4	112	0.41	0.012	13.2	4	0.72	9.6	**13.34**	1.25		
	#3	0.836	1.3	0.546	1.8	149	0.373	2.4	101	0.68	0.006	18.0	2	0.71	10.9	**15.38**	1.48		
14M25	#1	4.983	0.8	3.415	1.8	404	1.977	2.4	234	0.58	0.042	9.0	5	0.82	10.6	**12.95**	0.84	**13.0**	0.8
14M26	#1	0.852	1.0	0.559	1.8	248	0.102	2.4	45	0.18	0.008	15.4	4	0.71	12.10	**17.04**	1.63	**16.5**	0.8
	#2	2.999	0.9	1.674	1.8	262	1.063	2.4	166	0.64	0.042	10.5	7	0.81	12.89	**15.91**	1.07		
14M27	#1	7.941	0.9	3.845	1.8	258	0.771	2.4	52	0.20	0.039	10.8	3	0.83	16.32	**19.66**	1.24	**19.9**	0.2
	#2	2.554	0.9	1.231	1.8	229	0.615	2.4	114	0.50	0.039	11.5	7	0.76	15.35	**20.20**	1.63		
	#3	2.108	0.9	1.099	1.8	277	0.163	2.4	41	0.15	0.014	14.7	4	0.77	15.34	**19.92**	1.57		
14M29	#1	19.300	0.8	9.024	1.8	1756	1.307	2.4	254	0.14	0.016	19.0	3	0.84	17.11	**20.37**	1.24	**24.6**	2.1
	#2	7.266	0.8	3.088	1.8	652	0.264	2.4	56	0.09	0.040	11.3	8	0.72	19.08	**26.51**	2.44		
	#3	9.940	0.9	3.583	1.8	377	0.617	2.4	65	0.17	0.067	10.1	7	0.82	22.05	**26.89**	1.77		
14M30	#1	3.482	1.2	1.544	1.8	367	0.142	2.4	34	0.09	0.006	20.6	1	0.71	18.3	**25.73**	2.48	**25.7**	0.9
	#2	2.879	1.2	1.186	1.8	299	0.113	2.4	28	0.09	0.004	22.9	1	0.74	19.6	**26.55**	2.35		
	#3	13.137	1.1	5.219	1.8	467	1.204	2.4	108	0.23	0.091	5.3	8	0.80	19.7	**24.69**	1.78		
14M31	#1	1.476	1.2	0.812	1.8	231	0.180	2.4	51	0.22	0.013	10.2	4	0.76	14.3	**18.80**	1.56	**20.0**	1.6
	#2	8.919	1.1	4.403	1.8	737	0.580	2.4	97	0.13	0.108	5.0	18	0.77	16.3	**21.11**	1.69		
14M32	#1	2.982	0.9	2.494	1.8	1012	0.733	2.4	298	0.29	0.101	9.6	41	0.69	9.26	**13.42**	1.34	**14.5**	0.6
	#2	0.328	1.2	0.199	1.9	55	0.227	2.4	63	1.14	0.012	13.3	3	0.75	10.75	**14.34**	1.21		
	#3	0.724	1.1	0.529	1.8	235	0.081	2.5	36	0.15	0.004	22.9	2	0.70	10.94	**15.62**	1.54		
14M34	#1	5.532	0.8	2.304	1.8	594	3.831	2.4	988	1.66	0.028	11.5	7	0.77	14.25	**18.51**	1.42	**15.5**	1.6
	#2	0.581	1.1	0.439	1.8	72	0.106	2.4	17	0.24	0.010	15.8	2	0.70	10.37	**14.81**	1.46		
	#3	0.402	1.1	0.332	1.9	166	0.130	2.4	65	0.39	0.006	22.0	3	0.69	9.16	**13.27**	1.34		
14M35	#1	1.398	0.9	0.944	1.8	248	0.849	2.4	223	0.90	0.241	9.6	63	0.77	10.09	**13.10**	1.01	**15.7**	3.6
	#2	3.577	0.9	1.806	1.8	340	1.261	2.4	238	0.70	0.216	9.6	41	0.77	14.06	**18.26**	1.41		
	#3	1.636	0.9	0.753	1.8	604	0.260	2.4	208	0.34	0.025	11.3	20	0.64	16.61	**25.96***	2.97		
14M36	#1	0.429	1.1	0.314	1.9	207	0.155	2.4	102	0.49	0.011	14.2	7	0.67	10.13	**15.12**	1.62	**15.3**	1.1
	#2	1.622	0.9	1.170	1.8	231	0.396	2.4	78	0.34	0.013	13.6	3	0.79	10.63	**13.46**	0.99		
	#3	2.672	0.9	1.409	1.8	200	0.757	2.4	108	0.54	0.035	10.9	5	0.80	13.92	**17.40**	1.22		
14M37	#1	0.936	1.0	0.636	1.8	195	0.325	2.4	100	0.51	0.029	11.3	9	0.76	10.87	**14.30**	1.16	**14.8**	0.3
	#2	1.546	0.9	1.151	1.8	553	0.359	2.4	172	0.31	0.004	22.2	2	0.70	10.35	**14.79**	1.44		
	#3	2.378	0.9	1.691	1.8	529	0.297	2.4	93	0.18	0.005	20.4	2	0.73	11.18	**15.32**	1.37		
14M39	#1	1.810	1.3	1.132	1.8	266	0.517	2.4	121	0.46	0.101	5.6	24	0.71	11.9	**16.81**	1.62	**21.0**	5.9
	#2	4.275	1.2	1.802	1.8	366	0.851	2.4	173	0.47	0.059	6.2	12	0.70	17.7	**25.22**	2.48		
14M41	#1	3.125	1.2	2.314	1.8	286	0.613	2.4	76	0.27	0.006	16.4	1	0.81	10.5	**12.99**	0.91	**12.2**	0.7
	#2	0.909	1.3	0.810	1.8	258	0.228	2.4	73	0.28	0.003	25.8	1	0.73	8.7	**11.93**	1.09		
	#3	1.773	0.9	1.576	1.8	422	0.484	2.4	129	0.31	0.035	10.5	9	0.74	8.7	**11.74**	1.02		

Ejection correction (Ft): correction factor for alpha-ejection (according to Farley et al., 1996 and Hourigan et al., 2005). Uncertainty of the single-grain ages includes both the analytical uncertainty and the estimated uncertainty of the ejection correction. Sample age is the unweighted average age of all Ft-corrected (U-Th)/He ages. Results from aliquots marked with asterisk are not considered in the calculation of the sample age.

temperature of 10 °C, we determined exhumation rates from the cooling ages of mineral pairs. We calculated the exhumation rates by dividing cooling rates with an estimated value for the paleo-geothermal gradient. At present, the average surface heat flow of ~110 mW/m^2 in the Menderes Massif (Ilkişik, 1995) and heat flow models for the continental crust (Chapman and Furlong, 1992) indicate an average geothermal gradient of about 40 °C/km. During periods of extension however, the geothermal gradient may have increased to values of 50 °C/km or more (cf. Foster et al., 1991; Lund et al., 1993). For instance, Foster et al. (1991) calculated a geo-thermal gradient of 50 ± 20 °C/km for the Mojave extensional belt and Blackwell (1983) reported a high geothermal gradient of about 50 °C/km in the extensional Basin-and-Range Province. Based on geophysical data, the geothermal gradient for western Anatolia was calculated to range between 50 and 70 °C/km (Dolmaz et al., 2005). Thermal-kinematic modelling of low-angle normal faults indicates that within a few kilometres around the fault, the geothermal gradients in the hanging wall as well as the footwall are spatially invariant (e.g. Grasemann and Dunkl, 2003). To account for the above mentioned uncertainties of the paleo-geothermal gradient, we calculated exhumation rates for three different geothermal gradients of 30, 50, and 70 °C/km for the three sample groups defined above (Fig. 6a–i). For each of these three scenarios alternating phases of relatively fast and slow exhumation can be recognized and will be discussed in Section 5.1.

4.2. Results from cosmogenic ^{10}Be analysis

The erosion rates determined for the eight catchments in the Aydın block and the Küçük Menderes Graben range from ~50 to ~400 mm/kyr and are shown in Fig. 4. Blank-corrected ^{10}Be concentrations of the samples, production rates due to spallation and muons, and spatially integrated erosion rates for the respective catchments are presented in Table 6. The lowest erosion rates of 54 ± 5 and 64 ± 6 m/Myr were obtained for the two small catchments that are entirely located in augen gneisses of the Çine nappe at the eastern end of the Küçük Menderes Graben. These rates can be explained by the low erodibility of the coarse-grained orthogneisses and the rather low mean hillslope angles of the two catchments of ~16° and ~18°, respectively (Table 6). The sediment samples from the six larger catchments in the Aydın block yielded higher, albeit quite variable erosion rates between 84 ± 8 and 390 ± 39 m/Myr. The faster erosion documented for these catchments likely reflects the higher erodibility of the fragile mica schists and the generally steeper hillslopes of these catchments, which have mean hillslope

Table 5
Results of apatite (U-Th)/He geochronology.

Sample	Aliq.	He Vol. (10^{-9} cm^3)	1σ (%)	^{238}U Mass (ng)	1σ (%)	Conc. (ppm)	^{232}Th Mass (ng)	1σ (%)	Conc. (ppm)	Th/U ratio	Sm Mass (ng)	1σ (%)	Conc. (ppm)	Ejection correction	Uncorr. age (Ma)	FT-corr. age (Ma)	2σ (Ma)	Sample age (Ma)	2se (Ma)
14M23	#1	0.032	3.3	0.019	3.4	3.9	0.004	4.0	0.9	0.23	0.680	6.4	139	0.73	10.25	**14.04**	1.67	**17.5**	1.7
	#2	0.014	4.8	0.006	8.5	2.9	0.002	5.7	1.1	0.37	0.263	6.7	121	0.65	12.64	**19.44**	3.60		
	#3	0.047	2.6	0.022	3.0	4.2	0.006	3.7	1.1	0.26	0.861	6.0	161	0.66	12.55	**19.02**	2.37		
14M29	#1	0.295	1.2	0.120	1.9	14.4	0.022	2.9	2.7	0.19	1.998	5.8	240	0.80	17.19	**21.49**	1.56	**21.9**	1.2
	#2	0.423	1.1	0.163	1.8	17.6	0.031	2.7	3.3	0.19	2.204	5.8	238	0.77	18.59	**24.15**	1.92		
	#3	0.365	1.2	0.153	1.8	14.1	0.048	2.6	4.4	0.31	2.543	5.8	235	0.81	16.31	**20.13**	1.41		
14M31	#1	0.131	1.5	0.615	1.8	56.5	0.277	2.4	25.4	0.45	0.650	6.2	60	0.81	1.58	**1.95**	0.14	**1.6**	0.2
	#2	0.163	1.5	1.190	1.8	79.2	0.036	2.7	2.4	0.03	0.720	6.0	48	0.80	1.12	**1.40**	0.11		
	#3	0.171	1.4	1.190	1.8	79.4	0.058	2.6	3.9	0.05	0.771	6.0	51	0.80	1.17	**1.46**	0.11		
14M34	#1	0.001	12.3	0.002	31.5	0.6	0.002	7.7	0.7	1.12	0.035	13.6	12	0.75	2.10	**2.81**	1.40	**3.0**	0.3
	#2	0.010	5.8	0.028	2.6	7.1	0.029	2.7	7.1	1.00	0.149	7.2	37	0.72	2.28	**3.16**	0.47		
14M35	#1	0.008	6.3	0.011	5.2	6.7	0.007	3.7	4.3	0.64	0.076	9.1	48	0.65	5.14	**7.90***	1.45	**3.0**	0.3
	#2	0.027	3.6	0.081	1.9	11.6	0.056	2.6	8.0	0.69	0.318	6.5	46	0.77	2.29	**2.98**	0.31		
14M37	#1	0.013	5.1	0.010	5.5	4.2	0.018	3.0	7.3	1.75	0.055	9.3	23	0.76	7.39	**9.73**	1.41	**9.7**	1.4
14M40	#1	0.001	11.7	0.008	7.1	2.7	0.003	5.2	0.8	0.31	0.295	9.4	95	0.68	0.48	**0.70**	0.19	**0.5**	0.1
	#2	0.001	12.2	0.014	4.6	3.9	0.010	3.4	2.8	0.71	0.090	10.1	26	0.68	0.25	**0.37**	0.10		
	#3	0.001	12.2	0.020	3.4	9.1	0.007	3.6	3.2	0.35	0.028	13.1	13	0.66	0.29	**0.43**	0.12		

Ejection correction (Ft): correction factor for alpha-ejection (according to Farley et al., 1996). Uncertainty of the single-grain ages includes both the analytical uncertainty and the estimated uncertainty of the ejection correction. Sample age is the unweighted average age of all Ft-corrected (U-Th)/He ages (see: standard error). Results from aliquots marked with asterisk are not considered in the calculation of the sample age.

angles between 20 and 29 degrees (Table 6). The integration times of our eight samples range from ~1.5 to ~11 ka (Table 6).

5. Interpretation and discussion

5.1. Late Miocene/Pliocene to Oligocene cooling pattern of the Aydın block

As discussed earlier, the geothermal gradient in regions of active extension is relatively high, compared to stable regions (e.g. Foster et al., 1991). Therefore we consider a geothermal gradient of more than 30 °C/km as the most realistic scenario. In the following discussion we only refer to exhumation rates calculated for a geothermal gradient of 50 °C/km (Fig. 6b, e, h), however, we cannot exclude the possibility of a temporally higher gradient, for instance due to local fluid circulation near active faults.

The new thermochronological data from the Aydın block and the Küçük Menderes Graben define three groups of samples with different cooling paths and exhumation histories (Fig. 6). In particular, the data reveal two phases of footwall exhumation during the Miocene/Pliocene and the middle Miocene, respectively. The first group is defined by the youngest AFT and AHe ages from the southern flank of the Aydın block, which range between ~6 and ~3 Ma (Fig. 7). The exhumation rate of ~0.43 km/Myr for the latest Miocene and Pliocene (Fig. 6b) was likely caused by slip on the Büyük Menderes detachment fault and consequent tectonic denudation of the fault footwall. The link between footwall exhumation and detachment faulting is supported by K-Ar data from a fault gouge sample of the Büyük Menderes detachment that yielded ages between ~5 and ~3 Ma for three different grain size fractions (Hetzel et al. (2013), sample 09Me-NM01). These data corroborate the interpretation of Gessner et al. (2001a), who inferred rapid

Table 6
^{10}Be concentrations, production rates, and catchment-wide erosion rates in the central Menderes Massif, Turkey.

Sample	Latitude (WGS 84) (°N)	Longitude (WGS 84) (°E)	Sample elevation (m)	Mean catchment elevation[a] (m)	Mean hillslope angle of catchment[a] (°)	Topographic shielding factor[a] –	Production rate[a] (Spallation) (at/g/yr)	Production rate[a] (Muons) (at/g/yr)	^{10}Be concentration[b] (10^4 at/g)	Erosion rate[c] (mm/kyr)	Internal uncertainty (1σ) (mm/kyr)	External uncertainty (1σ) (mm/kyr)	Time scale (kyr)
14T5	38.1843	28.0838	174	270	15.7	0.9984	5.20	0.198	7.86 ± 0.39	**64.3**	±3.3	±5.6	9.3
14T7	38.0732	27.9323	416	887	24.3	0.9933	8.53	0.244	2.99 ± 0.18	**254**	±15	±24	2.4
14T8	38.0703	28.0990	398	1127	20.1	0.9955	10.28	0.264	10.25 ± 0.51	**83.6**	±4.2	±7.5	7.2
14T9	38.0752	28.0565	402	1100	28.8	0.9871	9.98	0.262	5.39 ± 0.29	**157.8**	±8.5	±14.3	3.8
14T12	38.1849	28.0870	185	345	17.5	0.9978	5.54	0.203	9.66 ± 0.41	**54.2**	±2.4	±4.5	11
14T13	37.9342	28.1713	232	1011	23.0	0.9917	9.35	0.254	7.01 ± 0.31	**114.4**	±5.2	±9.8	5.2
14T14	37.9593	28.0818	359	968	25.3	0.9914	9.05	0.251	2.05 ± 0.14	**390**	±28	±39	1.5
14T15	37.9716	28.0102	487	998	25.5	0.9909	9.25	0.253	4.36 ± 0.22	**184.1**	±9.3	±16.3	3.3

[a] The mean elevation of the catchments, their mean hillslope angles, and the topographic shielding factors were calculated using a 30 m Aster Digital Elevation Model. We calculated the topographic shielding factor with the MATLAB script of Greg Balco (http://depts.washington.edu/cosmolab/shielding.m). The ^{10}Be production rates were calculated with the CRONUS-Earth ^{10}Be–^{26}Al calculator (Balco et al., 2008; http://hess.ess.washington.edu/; version 2.2), using the time-invariant production rate scaling model of Lal (1991)–Stone (2000).

[b] Blank-corrected ^{10}Be concentrations. The uncertainty of the ^{10}Be concentration includes the error of the blank correction and the propagated error of the analytical uncertainty. The analytical error (1σ) takes into account the error based on counting statistics, the scatter of the repeated measurement of the same sample, as well as the uncertainty of the standard normalization. ^{10}Be concentrations were measured by AMS using the compact ETH Zurich Tandy system (Christl et al., 2013). Measured ^{10}Be/^{9}Be ratios are normalized to the secondary standard S2007N with a nominal ^{10}Be/^{9}Be ratio of 28.1×10^{-12} (Kubik and Christl, 2010), considering the ^{10}Be half-life of 1.387 ± 0.012 Ma (Chmeleff et al., 2010; Korschinek et al., 2010). The secondary standard has been calibrated relative to the primary standard ICN 01-5-1 (Nishiizumi et al., 2007; Kubik and Christl, 2010).

[c] Erosion rates were calculated with the CRONUS-Earth ^{10}Be–^{26}Al online calculator (Balco et al., 2008; http://hess.ess.washington.edu/; version 2.2). Internal uncertainties (1σ) include the analytical uncertainty and the error of the blank correction, whereas external uncertainties (1σ) also include the systematic uncertainty of the sea-level high-latitude production rate. Note that the 2.7 % error (1σ) associated with the ^{10}Be/^{9}Be ratio of the standard S2007N is also included in the external uncertainty (Kubik and Christl, 2010). For the calculation of the catchment-wide erosion rates, we used a density of 2.5 g/cm^3 and the mean elevation of the catchments. The time over which the erosion rate integrates is calculated by dividing the absorption depth scale of 60 cm by the erosion rate.

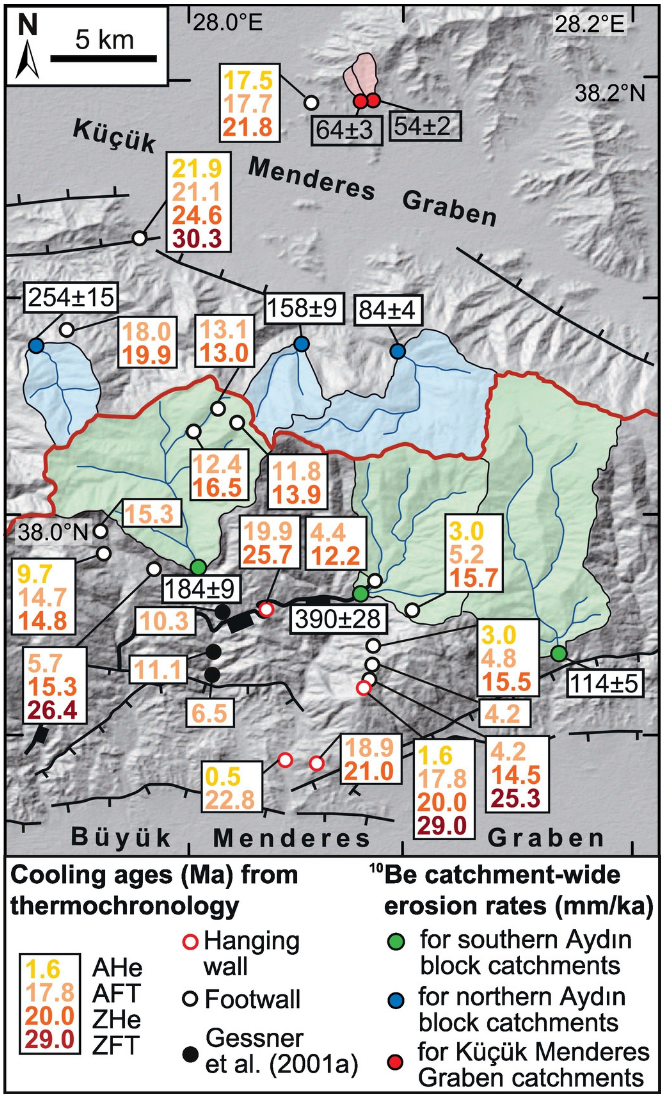

Fig. 4. Shaded-relief map of the study area with cooling ages derived from thermochronology and catchment-wide erosion rates (black numbers) based on cosmogenic ^{10}Be concentrations of stream sediments.

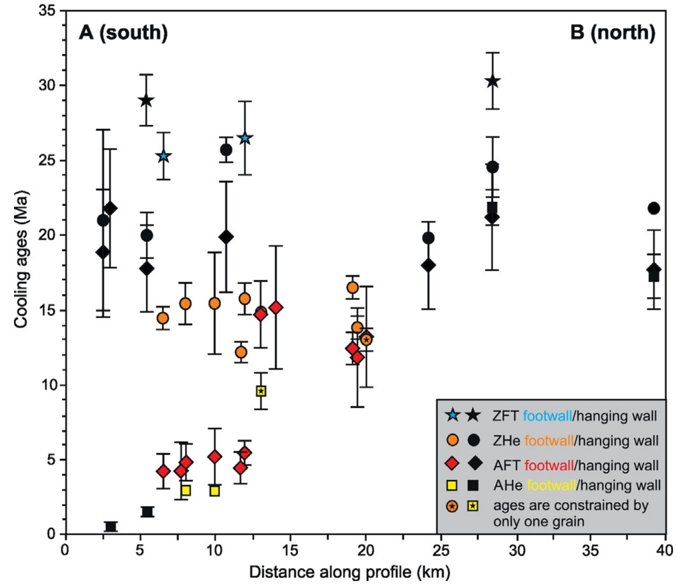

Fig. 5. Cooling ages from this study plotted versus distance along the profile A to B (for location see Fig. 2a).

cooling and coeval normal faulting on the Büyük Menderes and Gediz detachment faults in the Pliocene based on thermochronological data from the Gediz detachment only. The samples from the first group have ZFT ages of ~25 Ma and ZHe ages between 16 and 12 Ma, which are significantly older than their respective AFT and AHe ages and indicate an exhumation rate of ~0.1 km/Myr before ~5 Ma (Fig. 6b).

The samples from the second group are footwall samples from the central and northern part of the Aydın block and display early to middle Miocene ZHe and AFT ages and one AHe age of 9.7 ± 1.4 Ma. The exhumation rates derived from these ages decrease through time from ~0.9 to ~0.12 km/Myr between ~15 and ~10 Ma (Fig. 6e). These data document another phase of rather rapid cooling and exhumation in the middle Miocene, which may reflect a first phase of activity of the Büyük Menderes detachment fault. Such an older phase of detachment faulting was also inferred from a K-Ar age of 21.6 ± 0.6 Ma for a cataclasite from the Büyük Menderes detachment and a K-Ar fault gouge age of 22.3 ± 0.7 Ma for a normal fault in its hanging wall (Hetzel et al., 2013, samples 09Me-NM02 and 10Me18), however, more data are needed to bolster this interpretation and constrain the beginning of deformation. It is also important to note that during the first phase of detachment faulting the samples of group 1 (Fig. 6a–c) remained at temperatures above the partial annealing zone of fission tracks in apatite (i.e. 110–60 °C). Hence, the two distinct cooling paths recorded by the sample groups 1 and 2 indicate that two phases of relatively rapid exhumation were separated by a late Miocene period with little or no tectonic activity.

The third sample group – augen gneisses from the hanging wall (Çine nappe) exposed as klippen above the Büyük Menderes and in the Küçük Menderes Graben – gave the oldest thermochronological ages, indicating that these rocks cooled from ~240 to ~70 °C between ~30 Ma and ~18 Ma (Fig. 6h). This phase of cooling and exhumation occurred after the stacking of the Menderes nappes (e.g. Ring et al., 1999b; Gessner et al., 2013) and the Alpine prograde metamorphic evolution. Although the ZHe and AFT ages show some variability, the data seem to indicate that exhumation has accelerated in the late Oligocene/early Miocene from about ~0.16 to ~0.57 km/Myr (Fig. 6h). This interpretation is consistent with previous studies that reported a phase of rapid cooling during the late Oligocene and early Miocene for the Çine nappe (Gessner et al., 2001a; Ring et al., 2003). The subsequent exhumation occurred at a much lower mean rate of ~0.06 km/Myr (Fig. 6h). Only two samples (14M31, −40) from augen gneiss klippen in the vicinity of the Büyük Menderes graben yielded young AHe ages of 1.6 ± 0.2 Ma and 0.5 ± 0.1 Ma (Figs. 4, 5), which demonstrate that the final cooling of these klippen occurred in the Pleistocene. Similar observations were made at the Gediz detachment, where two AHe ages from augen gneiss klippen near the Gediz graben are ~2.9 and ~0.8 Ma (Buscher et al., 2013). As such young AHe ages are only found near the active graben structures, they probably record recent activity of graben-bounding normal faults. The presence of active normal faults is also evident from borehole logs in the Büyük Menderes Graben (e.g. Karamanderesi and Helvacı, 2003).

In summary, our new thermochronological data suggest that the Büyük Menderes detachment system was active during two phases that caused enhanced footwall cooling and exhumation. The first phase occurred during the middle Miocene and a second phase during the latest Miocene and Pliocene (Fig. 7). A similar temporal evolution is documented for the Gediz detachment fault, where detachment faulting was also operating in the mid-Miocene, as documented by U-Pb ages of 16.1 ± 0.2 Ma and 15.0 ± 0.3 Ma for two synextensional granodiorites that intruded the detachment-related mylonites (Glodny and Hetzel, 2007). This early stage of the Gediz detachment system was followed by enhanced cooling and footwall exhumation in the late Miocene and Pliocene, as indicated by apatite and zircon fission track and (U-Th)/He ages (Fig. 7) (Buscher et al., 2013). This younger

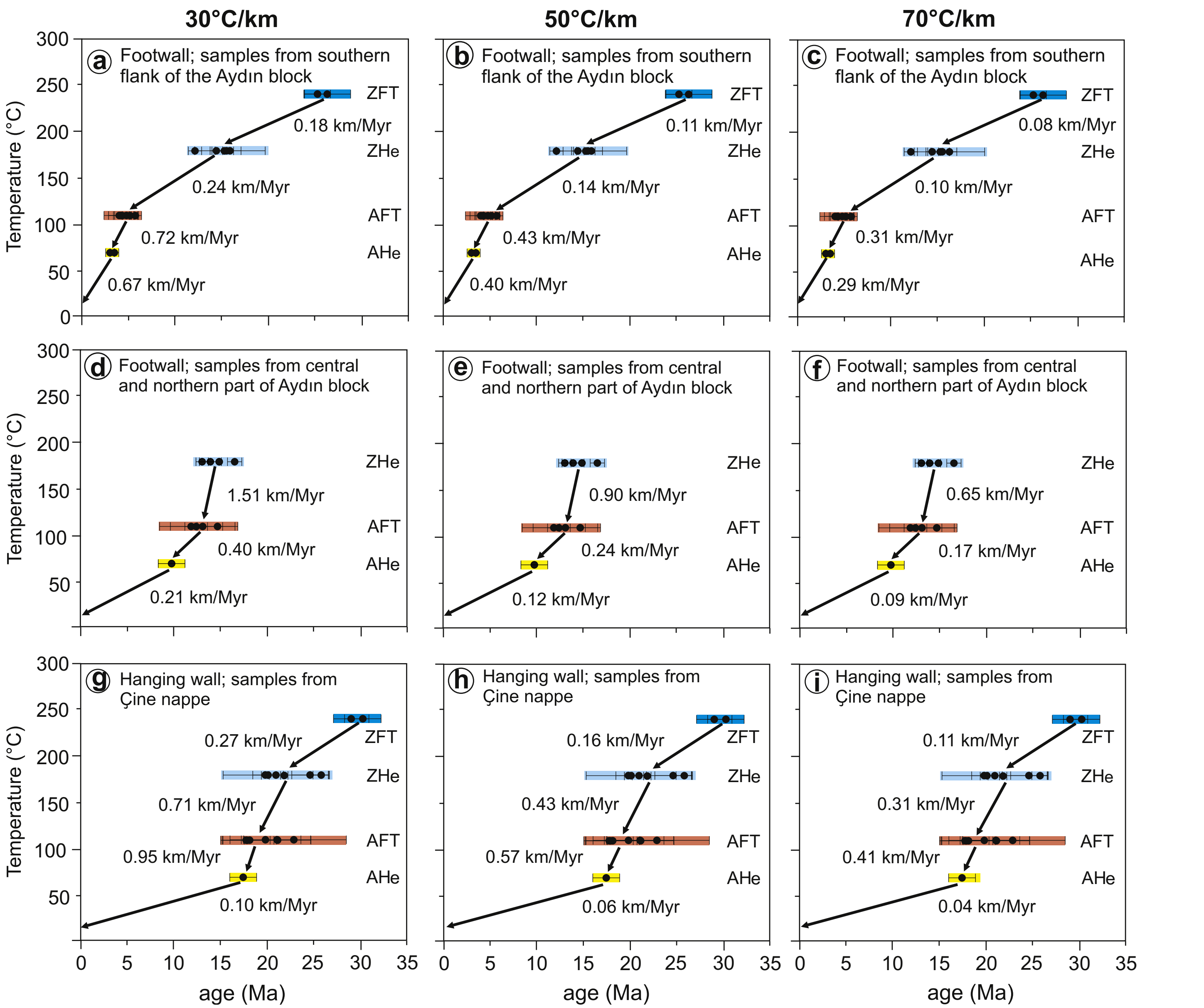

Fig. 6. (a–c) Average exhumation rates calculated from the cooling ages of mineral pairs for samples from the footwall (a–f) and hanging wall (g–i) of the Büyük Menderes detachment fault (see Section 4.1 for details). Left, middle and right columns are calculated with a geothermal gradient of 30, 50, and 70 °C/km, respectively.

phase of detachment faulting is supported by one Ar-Ar age of 7 ± 1 Ma for synkinematic white mica from the Gediz detachment (Lips et al., 2001). Hence, both detachment faults acted simultaneously in the middle Miocene as well as during the latest Miocene/Pliocene, as suggested by Gessner et al. (2001a). The similarity between two ZFT ages of ~25 Ma from the footwall and one ZFT age of ~29 Ma from hanging wall of the Büyük Menderes detachment (Fig. 5) indicates that this detachment fault was largely active at temperatures below ~250 °C. It was thus operating at a slightly shallower crustal level than the Gediz detachment. This interpretation is consistent with our field observations along the studied section, where features indicating a recrystallization of quartz (i.e. stretching lineations and mm-scale foliation in quartz veins) are conspicuously absent.

Our interpretation of two phases of detachment faulting, as described above, implies that the Büyük Menderes and Gediz detachments did not experience significant rotation over time. In other words, we argue that the detachments were active at a rather low angle during both phases of enhanced activity. Our interpretation is based on (i) the early to middle Miocene K-Ar ages on fault gouge and cataclasite from both detachments (Hetzel et al., 2013), (ii) the syntectonic emplacement of two granodiorites at the Gediz detachment at ~15 and ~16 Ma, respectively (Glodny and Hetzel, 2007) and (iii) the occurrence of early to middle Miocene sedimentary successions, which were interpreted as the infill of supra-detachment sedimentary basins (e.g. Purvis and Robertson, 2004; Sen and Seyitoğlu, 2009; Oner and Dilek, 2011; Oner and Dilek, 2013). Low-angle detachment faulting would be mechanically feasible (cf. Melosh, 1990; Forsyth, 1992; Collettini, 2011) and represents an efficient way to accommodate long-lasting extension (e.g., Wernicke, 1995; Jolivet et al., 2010; Morley, 2014). Note, however, that the actual geometry and dip of the detachments during the first phase of activity are poorly constrained and alternative interpretations are possible. In particular, the detachments could have been initially formed as high-angle normal faults in the early Miocene and could then have been reactivated in the Pliocene as rolling hinge detachment faults, which resulted in their present-day low dip (e.g., Gessner et al., 2001a; Ring et al., 2017). This interpretation would imply that the Büyük Menderes and Gediz detachments did not exist before the Pliocene (Ring et al., 2017). Note that a rolling-hinge style

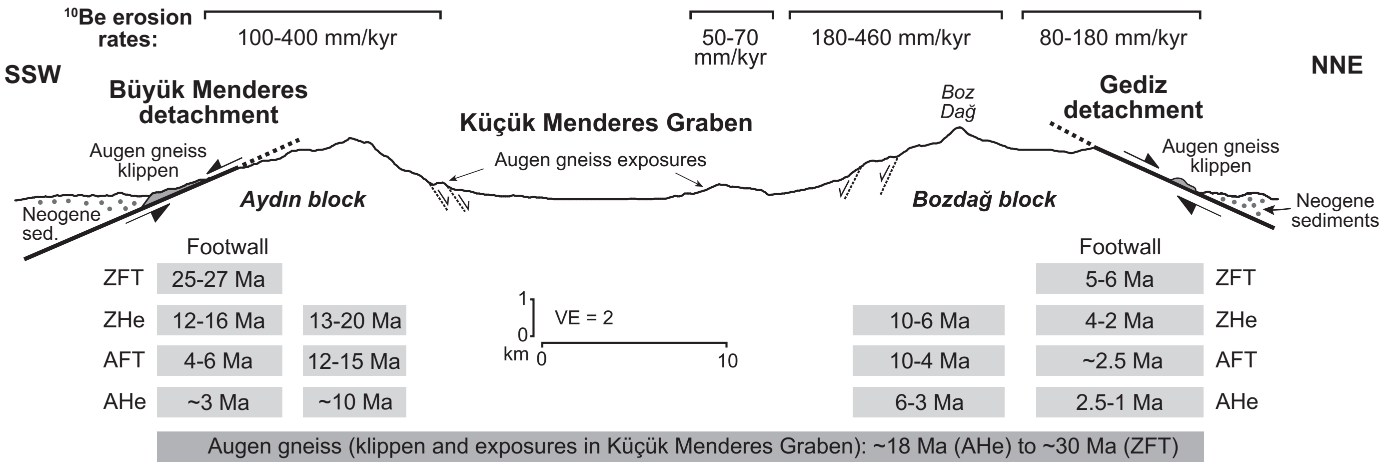

Fig. 7. Schematic profile across the central Menderes Massif summarizing cooling ages and catchment-wide erosion rates from this study and Buscher et al. (2013 and references therein).

of extension would also be mechanically feasible, as shown by numerical models (e.g., Lavier et al., 1999; Gessner et al., 2007).

5.2. Erosion pattern of the Aydın block and comparison with the Bozdağ block

The catchment-wide ^{10}Be-based erosion rates for the watersheds in the Aydın block range from ~100 to ~400 mm/kyr (Table 6, Fig. 7). Although the rates show some variability from catchment to catchment, they are quite similar on both the northern and southern mountain slopes of the Aydın block (Fig. 4). Given that the erosion rates integrate over several thousand years (Table 6), we infer that a relatively symmetric pattern of erosion has prevailed in the Aydın block during the Holocene. We argue that this pattern is likely controlled by the lithological similarities of the mica schists, which dominate both the Bozdağ and Bayındır nappes in the studied region of the Aydın block. The significantly lower erosion rates of ~54 and ~64 mm/kyr obtained for two catchments with resistant augen gneisses at the eastern end of the Küçük Menderes Graben corroborate the pronounced effect of lithology on erosion and are consistent with previous findings in other tectonically active mountain belts (Palumbo et al., 2010; Scharf et al., 2013b).

The symmetric erosion pattern in the Aydın block is in contrast to the spatial pattern of erosion documented for the Bozdağ block, where ^{10}Be-based erosion rates show an asymmetric distribution (Buscher et al., 2013). On the steep escarpment facing the Küçük Menderes Graben, erosion proceeds at rates that are about three times higher than those on the gently N-dipping mountain slope facing the Gediz Graben (Fig. 7). We attribute this marked difference in erosion rates to the presence of resistant, slowly-eroding cataclasites and quartzites in the footwall of the Gediz detachment, which constitutes a well-preserved geomorphic feature. The cataclasites associated with the Büyük Menderes detachment in the Aydın block are rather thin and resistant quartzites do not occur here, which is the reason why this detachment constitutes a less prominent feature in the landscape. In conclusion, despite having a similar relief, the lithological differences between the Gediz and Aydın blocks explain the contrasting geomorphologic appearance of the two detachment faults, which otherwise experienced a similar temporal and structural evolution.

The magnitude of the catchment-wide erosion rates of ~50 up to ~400 mm/kyr (or 0.05 to 0.4 km/Myr) as well as the presence of Neogene and Quaternary sediments on the Büyük Menderes detachment fault and in the adjacent graben suggests that, apart from normal faulting, erosion did also contribute to the exhumation of the metamorphic rocks in the central Menderes Massif. This hypothesis raises the question of how far back in time the erosion rates can be extrapolated. In this respect it is noteworthy that Holocene and late Pleistocene erosion rates estimated from the volumes of sediments in the deltas of the Büyük and Küçük Menderes rivers indicate no significant glacial-interglacial variations in erosion (Westaway, 1994). The Holocene erosion rates for these two river basins of 0.08 and 0.19 km/Myr, respectively, are similar to erosion rates of 0.09 and 0.15 km/Myr during the late Pleistocene (i.e. the period of 60–18 ka) (Westaway, 1994, his Tables 5 and 7). Importantly, the rates of 0.15 and 0.19 km/Myr for the entire Küçük Menderes basin agree quite well with our ^{10}Be-based rates of ~0.25, ~0.16, and ~0.08 km/Myr for the three large catchments that drain into the Küçük Menderes Graben (samples 14T7, −8, −9 in Table 6). These arguments suggest that erosion rates in the central Menderes Massif did probably not change significantly over the last glacial-interglacial cycle and may be at least roughly representative for the Quaternary period with its repeated glacial-interglacial cycles (cf. Lisiecki and Raymo, 2005). In order to better resolve the relative importance of erosion and normal faulting on the exhumation of the metamorphic rocks, the evolution of the topography through time needs to be better constrained, because local relief and hillslope angles constitute another major control on erosion apart from climate and lithology.

6. Conclusions

In this study we present new low-temperature thermochronological data and ^{10}Be-based catchment-wide erosion rates to quantify the interplay between extensional faulting and erosion in the central Menderes Massif in western Turkey. The fission-track and (U-Th)/He data document that the Büyük Menderes detachment fault, which defines the southern flank of the central Menderes Massif, experienced two phases of tectonic activity in the middle Miocene and in the latest Miocene/Pliocene. In contrast to the footwall, the hanging wall units cooled already in the early and middle Miocene to temperatures below ~70 °C. Erosion rates from cosmogenic ^{10}Be for catchments in the metamorphic rocks range mainly from 100 to 400 mm/kyr. If these erosion rates are representative for the last few million years, erosion may have made a significant contribution to the exhumation of the metamorphic rocks, even during the most rapid phases of exhumation. However, clarification of this issue requires data that allow to reconstruct the paleotopographic evolution of the Menderes Massif during the Late Cenozoic.

Acknowledgements

We thank A. Niehus (Universität Münster) for help in the lab during preparation of the ^{10}Be samples and V. Rapelius (Universität Münster) for ICP analyses. Funding for this study was provided by the Leibniz Universität Hannover (start-up funds to A. Hampel) and the German Research Foundation (grants HE 1704/18-1 and GL 724/7-1 to R. Hetzel and C. Glotzbach). Constructive reviews by M. Bernet, L. Jolivet, and U. Ring helped to improve the manuscript.

References

Ambraseys, N.N., 1971. Value of historical records of earthquakes. Nature 232, 375–379.

Armstrong, P.A., Ehlers, T.A., Chapman, D.S., Farley, K.A., Kamp, P.J.J., 2003. Exhumation of the central Wasatch Mountains, Utah: 1. Patterns and timing of exhumation deduced from low-temperature thermochronology data. J. Geophys. Res. 108 (2172). http://dx.doi.org/10.1029/2001JB001708.

Axen, G.J., Grove, M., Stockli, D., Lovera, O.M., Rothstein, D.A., Fletcher, J.M., Farley, K.A., Abbott, P.L., 2000. Thermal evolution of Monte Blanco dome: low-angle normal falting during Gulf of California rifting and late Eocene denudation of the eastern Peninsular Ranges. Tectonics 19, 197–212.

Balco, G., Stone, J.O., Lifton, N.A., Dunai, T.J., 2008. A complete and easily accessible means of calculating surface exposure ages or erosion rates from ^{10}Be and ^{26}Al measurements. Quat. Geochronol. 3, 174–195.

Bierman, R., Steig, E.J., 1996. Estimating rates of denudation using cosmogenic isotope abundances in sediment. Earth Surf. Process. Landf. 21, 125–139.

Blackwell, D.D., 1983. Heat flow in the northern Basin and Range province. In: Geothermal Resources Council (Ed.), The Role of Heat in the Development of Energy and Mineral Resources in the Northern Basin and Range Province, Special Report 13, pp. 81–92.

von Blanckenburg, F., 2006. The control mechanisms of erosion and weathering at basin scale from cosmogenic nuclides in river sediment. Earth Planet. Sci. Lett. 242, 224–239.

Bozkurt, E., 2000. Origin on N-S extensional tectonic in western Anatolia (Turkey): evidence from the Büyük Menderes Graben. In: Bozkurt, E., Winchester, J.A., Piper, J.D.A. (Eds.), Tectonics and Magmatism in Turkey and Its Surrounding Areas. The Geological Society of London, Special Publications 173, pp. 385–403.

Bozkurt, E., 2001. Late Alpine evolution of the central Menderes Massif, western Turkey. Int. J. Earth Sci. 89, 728–744.

Bozkurt, E., Oberhänsli, R., 2001. Menderes Massif (Western Turkey): structural, metamorphic and magmatic evolution – a synthesis. Int. J. Earth Sci. 89, 79–708.

Bozkurt, E., Sözbilir, H., 2004. Tectonic evolution of the Gediz Graben: field evidence for an episodic, two-stage extension in western Turkey. Geol. Mag. 141, 63–79.

Brichau, S., Ring, U., Ketcham, R.A., Carter, A., Stockli, D., Brunel, M., 2006. Constraining the long-term evolution of the slip rate for a major extensional fault system in the central Aegean, Greece, using thermochronology. Earth Planet. Sci. Lett. 241, 293–306.

Brichau, S., Ring, U., Carter, A., Bolhar, R., Monié, P., Stockli, D., Brunel, M., 2008. Timing, slip rate, displacement and cooling history of the Mykonos detachment footwall, Cyclades, Greece, and implications for the opening of the Aegean Sea basin. J. Geol. Soc. Lond. 165, 263–277.

Burtner, R., Nigrini, A., Donelick, R.A., 1994. Thermochronology of Lower Cretaceous source rocks in the Idaho-Wyoming Thrust belt. Bull. Am. Assoc. Pet. Geol. 78, 1613–1636.

Buscher, J.T., Hampel, A., Hetzel, R., Dunkl, I., Glotzbach, C., Struffert, A., Akal, C., Rätz, M., 2013. Quantifying rates of detachment faulting and erosion in the central Menderes Massif (western Turkey) by thermochronology and cosmogenic ^{10}Be. J. Geol. Soc. Lond. 170, 669–683.

Campani, M., Mancktelow, N., Seward, D., Rolland, Y., Müller, I., Guerra, I., 2010. Geochronological evidence for continuous exhumation through the ductile-brittle transition along a crustal-scale low-angle normal fault: Simplon Fault Zone, central Alps. Tectonics 29, TC3002. http://dx.doi.org/10.1029/2009TC002582.

Candan, O., Dora, O.Ö., Kun, N., Akal, C., Koraly, E., 1992. Allochthonous metamorphic units at the southern part of Aydın Mountains, Menderes Massif. Turk. Assoc. Pet. Geol. 4 (1), 93–110.

Candan, O., Dora, O.Ö., Oberhänsli, R., Çetinkaplan, M., Partzsch, J.H., Warkus, F.C., Dürr, S., 2001. Pan-African high-pressure metamorphism in the Precambrian basement of the Menderes Massif, western Anatolia, Turkey. Int. J. Earth Sci. 89, 793–811.

Candan, O., Oberhänsli, R., Dora, O.Ö., Çetinkaplan, M., Koralay, E., Rimmelé, G., Chen, F., Akal, C., 2011. Polymetamorphic evolution of the Pan-African basement and Palaeozoic-Early Tertiary Cover Series of the Menderes Massif. Bull. Mineral Res. Explor. 142, 121–163.

Çemen, I., Catlos, E.J., Gogus, O., Ozerdem, C., 2006. Post-collisional extensional tectonics and exhumation of the Menderes massif in the western Anatolia Extended Terrrane, Turkey. In: Dilek, Y., Pavlis, S. (Eds.), Postcollisional Tectonics and Magmatism in the Eastern Mediterranean Region. Geological Society of America, Special Papers 409, pp. 353–379.

Chapman, D.S., Furlong, K.P., 1992. Thermal state of the continental lower crust. In: Fountain, D.M., Arculus, R., Kay, R.W. (Eds.), Continental Lower Crust. Elsevier, Amsterdam, pp. 179–199.

Chmeleff, J., von Blanckenburg, F., Kossert, K., Jakob, D., 2010. Determination of the ^{10}Be half-life by multicollector ICP-MS and liquid scintillation counting. Nucl. Inst. Methods Phys. Res. B 268, 192–199.

Christl, M., Vockenhuber, C., Kubik, P.W., Wacker, L., Lachner, J., Alfimov, V., Synal, H.A., 2013. The ETH Zürich AMS facilities: performance parameters and reference materials. Nucl. Instrum. Methods Phys. Res., Sect. B 294, 29–38.

Çiftçi, N.B., Bozkurt, E., 2010. Structural evolution of the Gediz Graben, SW Turkey: temporal and spatial variation of the graben basin. Basin Res. 22, 846–873.

Collettini, C., 2011. The mechanical paradox of low-angle normal faults: current understanding and open questions. Tectonophysics 510, 253–268.

Dewey, J.F., 1988. Extensional collapse of orogens. Tectonics 7, 1123–1139.

Dokka, R.K., Mahaffie, M.J., Snoke, A.W., 1986. Thermochronologic evidence of major tectonic denudation associated with detachment faulting, Northern Ruby Mountains – East Humboldt Range, Nevada. Tectonics 5, 995–1006.

Dolmaz, M.N., Hisarli, Z.M., Ustaömer, T., Orbay, N., 2005. Curie point depths based on spectrum analysis of aeromagnetic data, west Anatolian extensional province, Turkey. Pure Appl. Geophys. 162, 571–590.

Donelick, R.A., Ketcham, R.A., Carlson, W.D., 1999. Variability of apatite fission track annealing kinetics II: crystallographic orientation effects. Am. Mineral. 84, 1224–1234.

Dunkl, I., 2002. TRAKKEY: a window program for calculation and graphical presentation of fission track data. Comput. Geosci. 28, 3–12.

Ehlers, T.A., Farley, K.A., 2003. Apatite (U-Th)/He thermochronometry: methods and applications to problems in tectonics and surface processes. Earth Planet. Sci. Lett. 206, 1–14.

Emre, T., 1996. The tectonic evolution of the Gediz graben. Geol. Bull. Turk. 39, 1–18.

Emre, T., Sözbilir, H., 1997. Field evidence for metamorphic core complex, detachment faulting and accommodation faults in the Gediz and Büyük Menderes Grabens, Western Anatolia. International Earth Science Colloquium on the Aegean and Surrounding Regions, Proceedings, 1995, 1, pp. 73–94.

Emre, T., Sözbilir, H., 2007. Tectonic evolution of the Kiraz Basin, Küçük Menderes Graben: evidence for compression/uplift-related basin formation overprinted by extensional tectonics in West Anatolia. Turk. J. Earth Sci. 16, 441–470.

Eyidoğan, H., Jackson, J., 1985. A seismological study of normal faulting in the Demirci, Alaşehir and Gediz earthquakes of 1969–70 in western Turkey: implications for the nature and geometry of deformation in the continental crust. Geophys. J. R. Astron. Soc. 81, 569–607.

Farley, K.A., 2000. Helium diffusion from apatite: general behavior as illustrated by Durango fluorapatite. J. Geophys. Res. 105, 2903–2914.

Farley, K.A., 2002. (U-Th)/He dating: techniques, calibrations and applications. Mineralogical Society of America. Rev. Mineral. Geochem. 47, 819–844.

Farley, K.A., Wolf, R.A., Silver, L.T., 1996. The effects of long alpha-stopping distances on (U-Th)/He ages. Geochim. Cosmochim. Acta 60, 4223–4229.

Fitzgerald, P.G., Fryxell, J.E., Wernicke, B.P., 1991. Miocene crustal extension and uplift in southeastern Nevada: constraints from fission track analysis. Geology 19, 1013–1016.

Flowers, R.M., Shuster, D.L., Farley, K.A., 2007. Radiation damage control on apatite (U-Th)/He dates from the Grand Canyon region, Colorado Plateau. Geology 35, 447–450.

Forsyth, D.W., 1992. Finite extension and low-angle normal faulting. Geology 20, 27–30.

Foster, D.A., Miller, D.S., Miller, C.F., 1991. Tertiary extension in the Old Woman Mountains area, California: evidence from apatite fission track analysis. Tectonics 10, 875–886.

Gautier, P., Brun, J.P., 1994. Ductile crust exhumation and extensional detachments in the central Aegean (Cyclades and Evvia islands). Geodin. Acta 7, 57–85.

Gessner, K., Ring, U., Lackmann, W., Passchier, C.W., Güngör, T., 1998. Structure and crustal thickening of the Menderes Massif, southwest Turkey, and consequences for large-scale correlations between Greece and Turkey. Bull. Geol. Soc. Greece 1, 145–152.

Gessner, K., Ring, U., Johnson, C., Hetzel, R., Passchier, C.W., Güngör, T., 2001a. An active bivergent rolling-hinge detachment system: Central Menderes metamorphic core complex in western Turkey. Geology 29, 611–614.

Gessner, K., Piazolo, S., Güngör, T., Ring, U., Kröner, A., Passchier, C.W., 2001b. Tectonic significance of deformation patterns in granitoid rocks of the Menderes nappes, Anatolide belt, southwest Turkey. Int. J. Earth Sci. 89, 766–780.

Gessner, K., Collins, A.S., Ring, U., Gungor, T., 2004. Structural and thermal history of polyorogenic basement: U-Pb geochronology of granitoid rocks in the southern Menderes Massif, Western Turkey. J. Geol. Soc. Lond. 161, 93–101.

Gessner, K., Wijns, C., Moresi, L., 2007. Significance of strain localization in the lower crust for structural evolution and thermal history of metamorphic core complexes. Tectonics 26, TC2012. http://dx.doi.org/10.1029/2004TC001768.

Gessner, K., Gallardo, L.A., Markwitz, V., Ring, U., Thomson, S.N., 2013. What caused the denudation of the Menderes Massif: review of crustal evolution, lithosphere structure, and dynamic topography in southwest Turkey. Gondwana Res. 24, 243–274.

Gleadow, A.J.W., 1981. Fission-track dating methods: what are the real alternatives? Nucl. Tracks 5, 3–14.

Gleadow, A.J.W., Duddy, I.R., 1981. A natural long-term track annealing experiment for apatite. Nucl. Tracks 5, 169–174.

Glodny, J., Hetzel, R., 2007. Precise U-Pb ages of syn-extensional Miocene intrusions in the central Menderes Massif, western Turkey. Geol. Mag. 144, 235–246.

Goethals, M.M., Hetzel, R., Niedermann, S., Wittmann, H., Fenton, C.R., Kubik, P.W., Christl, M., von Blanckenburg, F., 2009. An improved experimental determination of cosmogenic ^{10}Be/^{21}Ne and ^{26}Al/^{21}Ne production ratios in quartz. Earth Planet. Sci. Lett. 284, 187–198.

Granger, D.E., Kirchner, J.W., Finkel, R., 1996. Spatially averaged long-term erosion rates measured from in situ-produced cosmogenic nuclides in alluvial sediment. J. Geol. 104, 249–257.

Grasemann, B., Dunkl, I., 2003. Effects of the geometry of normal faulting on the near surface heat flow during extension: the example of the Rechnitz Metamorphic Core Complex (Austria). Mitt. Österr. Geol. Ges. 92, 87–103.

Grasemann, B., Schneider, D.A., Stockli, D.F., Iglseder, C., 2012. Miocene bivergent crustal extension in the Cyclades (Greece). Lithosphere 4, 23–39.

Green, P.F., Duddy, I.R., Gleadow, A.J.W., Tingate, P.R., Laslett, G.M., 1986. Thermal annealing of fission tracks in apatite 1. A qualitative description. Chem. Geol. 59, 237–253.

Guenthner, W.R., Reiners, P.W., Ketcham, R.A., Nasdala, L., Giester, G., 2013. Helium diffusion in natural zircon: radiation damage, anisotropy, and the interpretation of zircon (U-Th)/He thermochronology. Am. J. Sci. 313, 145–198.

Gürer, Ö.F., Sarıca-Filoreau, N., Özburan, M., Sangu, E., Doğan, B., 2009. Progressive development of the Büyük Menderes Graben based on new data, western Turkey. Geol. Mag. 146, 652–673.

Heineke, C., Hetzel, R., Akal, C., Christl, M., 2017. Lifespan of water reservoirs estimated from cosmogenic ^{10}Be in stream sediment. Water Resour. Res. (manuscript in revision).

Herman, F., Braun, J., Senden, T.J., Dunlap, W.J., 2007. (U-Th)/He thermochronometry: mapping 3D geometry using micro-X-ray tomography and solving the associated production-diffusion equation. Chem. Geol. 242, 126–136.

Hetzel, R., Reischmann, T., 1996. Intrusion of Pan-African gneisses in the southern Menderes massif and the age of cooling after Alpine ductile extensional deformation. Geol. Mag. 133, 565–572.

Hetzel, R., Ring, U., Akal, C., Troesch, M., 1995a. Miocene NNE-directed extensional unroofing in the Menderes Massif, southwestern Turkey. J. Geol. Soc. Lond. 152, 639–654.

Hetzel, R., Passchier, C.W., Ring, U., Dora, O.Ö., 1995b. Bivergent extension in orogenic belts: the Menderes Massif (southwestern Turkey). Geology 23, 455–458.

Hetzel, R., Romer, R.L., Candan, O., Passchier, C.W., 1998. Geology of the Bozdağ area, central Menderes massif, SW Turkey: Pan-African basement and Alpine deformation. Int. J. Earth Sci. 87, 394–406.

Hetzel, R., Zwingmann, H., Mulch, A., Gessner, K., Akal, C., Hampel, A., Güngör, T., Petschick, R., Mikes, T., 2013. Spatiotemporal evolution of brittle normal faulting and fluid infiltration in detachment fault systems: a case study from the Menderes Massif, western Turkey. Tectonics 32:1–13. http://dx.doi.org/10.1002/tect.20031.

Hourigan, J.K., Reiners, P.W., Brandon, M.T., 2005. U-Th zonation-dependent alpha-ejection in (U-Th)/He chronometry. Geochim. Cosmochim. Acta 69, 3349–3365.

Hurford, A.J., Green, P.F., 1983. The zeta age calibration of fission-track dating. Chem. Geol. 1, 285–317.

Ilkişik, O.M., 1995. Regional heat flow in western Anatolia using silica temperature estimates from thermal springs. Tectonophysics 244, 175–184.

Işik, V., Tekeli, O., Seyitoglu, G., 2004. The ^{40}Ar/^{39}Ar age of extensional ductile deformation and granitoid intrusion in the northern Menderes core complex: implications for the initiation of extensional tectonics in western Turkey. J. Asian Earth Sci. 23, 555–566.

Işik, V., Seyitoğlu, G., Çemen, I., 2003. Ductile-brittle transition along the Alaşehir detachment fault and its structural relationship with the Simav detachment fault, Menderes massif, western Turkey. Tectonophysics 374, 1–18.

Jolivet, L., Lecomte, E., Huet, B., Denéle, Y., Lacombe, O., Labrousse, L., Le Pourhiet, L., Mehl, C., 2010. The North Cycladic Detachment System. Earth Planet. Sci. Lett. 289, 87–104.

Karamanderesi, I.H., Helvacı, C., 2003. Geology and hydrothermal alteration of the Aydın-Salavatlı Geothermal Field, Western Anatolia, Turkey. Turk. J. Earth Sci. 12, 175–198.

Kohl, C.P., Nishiizumi, K., 1992. Chemical isolation of quartz for measurement of in-situ produced cosmogenic nuclides. Geochim. Cosmochim. Acta 56, 3583–3587.

Koralay, O.E., 2015. Late Neoproterozoic granulite facies metamorphism in the Menderes Massif, Western Anatolia/Turkey: implication for the assembly of Gondwana. Geodin. Acta 27, 244–266.

Koralay, O.E., Satir, M., Dora, O.Ö., 2001. Geochemical and geochronological evidence for Early Triassic calc-alkaline magmatism in the Menderes Massif, western Turkey. Int. J. Earth Sci. 89, 822–835.

Koralay, O.E., Candan, O., Akal, C., Dora, O.Ö., Chen, F., Satir, M., Oberhänsli, R., 2011. Geology and geochronology of the Pan-African and Triassic metagranitoids in the Menderes Massif, Western Anatolia, Turkey. Bull. Mineral Res. Explor. 142, 69–121.

Korschinek, G., Bergmaier, A., Faestermann, T., Gerstmann, U.C., Knie, K., Rugel, G., Wallner, A., Dillmann, I., Dollinger, G., von Gostomski, Ch.L., Kossert, K., Maiti, M., Poutivtsev, M., Remmert, A., 2010. A new value for the half-life of ^{10}Be by heavy-ion elastic recoil detection and liquid scintillation counting. Nucl. Inst. Methods Phys. Res. B 268, 187–191.

Kubik, P.W., Christl, M., 2010. ^{10}Be and ^{26}Al measurements at the Zurich 6 MV Tandem AMS facility. Nucl. Inst. Methods Phys. Res. B 268, 880–883.

Lal, D., 1991. Cosmic ray labeling of erosion surfaces: in situ nuclide production rates and erosion models. Earth Planet. Sci. Lett. 104, 424–439.

Lavier, L.L., Buck, W.R., Poliakov, A.N.B., 1999. Self-consistent rolling-hinge model for the evolution of large-offset low-angle normal faults. Geology 27, 1127–1130.

Lee, J., Lister, G.S., 1992. Late Miocene ductile extension and detachment faulting, Mykonos, Greece. Geology 20, 121–124.

Lippolt, H.J., Leitz, M., Wernicke, R.S., Hagerdon, B., 1994. (Uranium + thorium)/helium dating of apatite: experience with samples from different geochemical environments. Chem. Geol. 112, 179–191.

Lips, A.L.W., Cassard, D., Sözbilir, H., Yilmaz, H., Wijbrans, J.R., 2001. Multistage exhumation of the Menderes Massif, western Anatolia (Turkey). Int. J. Earth Sci. 89, 781–792.

Lisiecki, L.E., Raymo, M.E., 2005. A Pliocene-Pleistocene stack of 57 globally distributed benthic δ^{18}O records. Paleoceanography 20, PA1003. http://dx.doi.org/10.1029/2004PA001071.

Lister, G.S., Davis, G.A., 1989. The origin of metamorphic core complexes and detachment faults formed during Tertiary continental extension in the northern Colorado River region, U.S.A. J. Struct. Geol. 11, 65–94.

Loos, S., Reischmann, T., 1999. The evolution of the southern Menderes Massif in SW Turkey as revealed by zircon dating. J. Geol. Soc. Lond. 156, 1021–1030.

Lund, K., Beard, L.S., Perry, W.J., 1993. Relation between extensional geometry of the northern Grant Range and oil occurrences in Railroad Valley, east-central Nevada. Am. Assoc. Pet. Geol. 77, 945–962.

Mancktelow, N.S., 1992. Neogene lateral extension during convergence in the Central Alps: evidence from interrelated faulting and backfolding around the Simplonpass (Switzerland). Tectonophysics 215, 295–317.

Melosh, H.J., 1990. Mechanical basis for low-angle normal faulting in the Basin and Range province. Nature 343, 331–335.

Morley, C.K., 2014. The widespread occurrence of low-angle normal faults in a rift setting: review of examples from Thailand, and implications for their origin and evolution. Earth Sci. Rev. 133, 18–42.

Naeser, C.W., 1978. Fission track dating. U.S. Geological Survey Open File Report 76–190 (31 pp.).

Nishiizumi, K., Imamura, M., Caffee, M.W., Southon, J.R., Finkel, R.C., McAninch, J., 2007. Absolute calibration of ^{10}Be AMS standards. Nucl. Inst. Methods Phys. Res. B 258, 403–413.

Oberhänsli, R., Candan, O., Dora, O.Ö., Dürr, S., 1997. Eclogites within the Menderes Massif/western Turkey. Lithos 41, 135–150.

Oner, Z., Dilek, Y., 2011. Supradetachment basin evolution during continental extension: the Aegean province of western Anatolia, Turkey. Geol. Soc. Am. Bull. 123, 2115–2141.

Oner, Z., Dilek, Y., 2013. Fault kinematics in supradetachment basin formation, Menderes core complex in western Turkey. Tectonophysics 608, 1394–1412.

Özer, S., Sözbilir, H., 2003. Presence and tectonic significance of Cretaceous rudist species in the so-called Permo-Carboniferous Göktepe Formation, central Menderes metamorphic massif, western Turkey. Int. J. Earth Sci. 92, 397–404.

Palumbo, L., Hetzel, R., Tao, M., Li, X., 2010. Topographic and lithologic control on catchment-wide denudation rates derived from cosmogenic ^{10}Be in two mountain ranges at the margin of NE Tibet. Geomorphology 117, 130–142.

Purvis, M., Robertson, A., 2004. A pulsed extension model for the Neogene–Recent E–W-trending Alaşehir Graben and the NE–SW-trending Selendi and Gördes Basins, western Turkey. Tectonophysics 391, 171–201.

Rahn, M.K., Brandon, M.T., Batt, G.E., Garver, J.I., 2004. A zero-damage model for fission-track annealing in zircon. Am. Mineral. 89, 473–484.

Regnier, J.L., Ring, U., Passchier, C.W., Gessner, K., Güngör, T., 2003. Contrasting metamorphic evolution of metasedimantary rocks from the Çine and Selimiye nappes in the Anatolide belt, western Turkey. J. Metamorph. Geol. 21, 699–721.

Reiners, P.W., 2005. Zircon (U-Th)/He thermochronometry. Rev. Mineral. Geochem. 58, 151–179.

Reiners, P.W., Brandon, M.T., 2006. Using thermochronology to understand orogenic erosion. Annu. Rev. Earth Planet. Sci. 34, 419–466.

Reiners, P.W., Ehlers, T.A. (Eds.), 2005. Low-temperature thermochronology: techniques, interpretations, and applications. Rev. Mineral. Geochem. (622 pp.).

Reiners, P.W., Zhou, Z., Ehlers, T.A., Xu, C., Brandon, M.T., Donelick, R.A., Nicolescu, S., 2003. Post-orogenic evolution of the Dabie Shan, eastern China, from (U-Th)/He and fission track thermochronology. Am. J. Sci. 303, 489–518.

Reiners, P.W., Spell, T.I., Nicolescu, S., Zanetti, K., 2004. Zircon (U-Th)/He thermochronometry: He diffusion and comparisons with ^{40}Ar/^{39}Ar dating. Geochim. Cosmochim. Acta 68, 1857–1887.

Ring, U., Brandon, M.T., Lister, G.S., Willett, S.D., 1999a. Exhumation processes. In: Ring, U., Brandon, M.T., Lister, G.S., Willett, S.D. (Eds.), Exhumation Processes: Normal Faulting, Ductile Flow, and Erosion. The Geological Society of London, Special Publications 154, pp. 1–27.

Ring, U., Gessner, K., Güngör, T., Passchier, C.S., 1999b. The Menderes Massif of western Turkey and the Cycladic Massif in the Aegean – do they really correlate? J. Geol. Soc. Lond. 156, 3–6.

Ring, U., Willner, A., Lackmann, W., 2001. Nappe stacking and clockwise versus anticlockwise pressure-temperature paths: an example from the Menderes nappes of western Turkey. Am. J. Sci. 301, 912–944.

Ring, U., Johnson, C., Hetzel, R., Gessner, K., 2003. Tectonic denudation of a Late Cretaceous-Tertiary collisional belt: regionally symmetric cooling patterns and their relation to extensional faults in the Anatolide belt of western Turkey. Geol. Mag. 140, 421–441.

Ring, U., Gessner, K., Thomson, S., 2017. Variations in fault-slip data and cooling history reveal corridor of heterogeneous backarc extension in the eastern Aegean Sea region. Tectonophysics 700–701, 108–130.

Rojay, B., Toprak, V., Demirci, C., Süzen, L., 2005. Plio-Quaternary evolution of the Küçük Menderes Graben Southwestern Anatolia, Turkey. Geodin. Acta 18, 317–331.

Satir, M., Friedrichsen, H., 1986. The origin and evolution of the Menderes Massif, W-Turkey: a rubidium/strontium and oxygen isotope study. Int. J. Earth Sci. 75, 703–714.

Schaffer, F., 1900. Das Maeanderthalbeben vom 20 September 1899. Mitteilungen der kaiserlichen-königlichen geographischen Gesellschaft Wien. vol. 43, pp. 221–230.

Scharf, A., Handy, M.R., Favaro, S., Schmid, S.M., Bertrand, A., 2013a. Modes of orogen-parallel stretching and extensional exhumation in response to microplate indentation and roll-back subduction (Tauern Window, Eastern Alps). Int. J. Earth Sci. 102, 1627–1654.

Scharf, T.E., Codilean, A.T., de Wit, M., Jansen, J.D., Kubik, P.W., 2013b. Strong rocks sustain ancient postorogenic topography in southern Africa. Geology 41, 331–334.

Schmidt, A., Pourteau, A., Candan, O., Oberhänsli, R., 2015. Lu-Hf geochronology on cm-sized garnets using microsampling: new constraints on garnet growth rates and duration of metamorphism during continental collision (Menderes Massif, Turkey). Earth Planet. Sci. Lett. 432, 24–35.

Selverstone, J., 1988. Evidence for east-west crustal extension in the Eastern Alps. Implications for unroofing history of the Tauern Window. Tectonics 7, 87–105.

Sen, S., Seyitoğlu, G., 2009. Magnetostratigraphy of early-middle Miocene deposits from east-west trending Alaşehir and Büyük Menderes grabens in western Turkey, and its tectonic implications. In: van Hinsbergen, D.J.J., Edwards, M.A., Govers, R. (Eds.), Collision and Collapse at the Africa-Arabia-Eurasia Subduction Zone. The Geological Society of London, Special Publications 311, pp. 321–342.

Şengör, A.M.C., Satir, M., Akkör, R., 1984. Timing of tectonic events in the Menderes Massif, western Turkey: implications for tectonic evolution and evidence for Pan-African basement in Turkey. Tectonics 3, 693–707.

Seyitoğlu, G., Scott, B.C., 1991. Late Cenozoic crustal extension and basin formation in west Turkey. Geol. Mag. 128, 155–166.

Sözbilir, H., Sarı, B., Uzel, B., Sümer, Ö., Akkiraz, S., 2011. Tectonic implications of transtensional supradetachment basin development in an extension-parallel transfer zone: the Kocaçay Basin, western Anatolia, Turkey. Basin Res. 23, 423–448.

Stone, J.O., 2000. Air pressure and cosmogenic isotope production. J. Geophys. Res. 105, 23753–23759.

Sümer, Ö., 2015. Evidence for the reactivation of a pre-existing zone of weakness and its contributions to the evolution of the Küçük Menderes Graben: a study of the Ephesus Fault, Western Anatolia, Turkey. Geodin. Acta 27, 130–154.

Thomson, S.N., Ring, U., 2006. Thermochronologic evaluation of postcollision extension in the Anatolide orogen, western Turkey. Tectonics 25, TC3005. http://dx.doi.org/10.1029/2005TC001833.

Wagner, G.A., van den Haute, P., 1992. Fission-track Dating. Kluwer Academic Publishers, The Netherlands (285 pp.).

Wernicke, B., 1995. Low-angle normal faults and seismicity: a review. J. Geophys. Res. 100, 20159–20174.

Wernicke, B., Axen, G.J., Snow, J.K., 1988. Basin and range extensional tectonics at the latitude of Las Vegas, Nevada. Geol. Soc. Am. Bull. 100, 1738–1757.

Westaway, R., 1994. Evidence for dynamic coupling of surface processes with isostatic compensation in the lower crust during active extension in western Turkey. J. Geophys. Res. 99, 203–223.

Wolf, R.A., Farley, K.A., Silver, L.T., 1996. Helium diffusion and low temperature thermochronology of apatite. Geochim. Cosmochim. Acta 60, 4231–4240.

Wolf, R.A., Farley, K.A., Kass, D.M., 1998. Modeling of the temperature sensitivity of the apatite (U-Th)/He thermochronometer. Chem. Geol. 148, 105–114.

Yılmaz, Y., Genç, S.C., Gürer, F., Bozcu, M., Yılmaz, Z., Karacik, S., Altunakynak, A., Elmas, A., 2000. When did the western Anatolian grabens begin to develop? In: Bozkurt, E., Winchester, J.A., Piper, J.D.A. (Eds.), Tectonics and Magmatism in Turkey and Surrounding Regions. The Geological Society of London, Special Publication 173, pp. 353–384

Zaun, P.E., Wagner, G.A., 1985. Fission-track stability in zircons under geological conditions. Nucl. Tracks 10, 303–307.

Zeitler, P.K., Herczeg, A.L., McDougall, I., Honda, M., 1987. U-Th-He dating of apatite: a potential thermochronometer. Geochim. Cosmochim. Acta 51, 2865–2868.

Zlatkin, O., Avigad, D., Gerdes, A., 2012. Evolution and provenance of Neoproterozoic basement and Lower Palaeozoic siliciclastic cover of the Menderes Massif (Western Taurides): coupled U-Pb-Hf zircon isotope geochemistry. Gondwana Res. 23, 682–700.